August 17, 2018

The SLUGGS Survey: The Inner Dark Matter Density Slope of the Massive Elliptical Galaxy NGC 1407

Asher Wasserman, *University of California, Santa Cruz*
Aaron J. Romanowsky, *San Jose State University*
Jean Brodie, *University of California, Santa Cruz*
Pieter G. van Dokkum, *Yale University*
Charlie Conroy, *Harvard University*, et al.

The SLUGGS Survey: The Inner Dark Matter Density Slope of the Massive Elliptical Galaxy NGC 1407

Asher Wasserman[1] , Aaron J. Romanowsky[2,3] , Jean Brodie[1,3] , Pieter van Dokkum[4] , Charlie Conroy[5] ,
Alexa Villaume[1] , Duncan A. Forbes[6] , Jay Strader[7] , Adebusola Alabi[3], and Sabine Bellstedt[6]
[1] Department of Astronomy & Astrophysics, University of California-Santa Cruz, Santa Cruz, CA 95064, USA; adwasser@ucsc.edu
[2] Department of Physics and Astronomy, San José State University, One Washington Square, San Jose, CA 95192, USA
[3] University of California Observatories, 1156 High Street, Santa Cruz, CA 95064, USA
[4] Astronomy Department, Yale University, New Haven, CT 06511, USA
[5] Department of Astronomy, Harvard University, Cambridge, MA 02138, USA
[6] Centre for Astrophysics & Supercomputing, Swinburne University, Hawthorn VIC 3122, Australia
[7] Center for Data Intensive and Time Domain Astronomy, Department of Physics and Astronomy, Michigan State University, East Lansing, MI 48824, USA
Received 2017 November 21; revised 2018 June 22; accepted 2018 July 5; published 2018 August 17

Abstract

We investigate the dark matter density profile of the massive elliptical galaxy, NGC 1407, by constructing spherically symmetric Jeans models of its field star and globular cluster systems. Two major challenges in such models are the degeneracy between the stellar mass and the dark matter halo profiles, and the degeneracy between the orbital anisotropy of the tracer population and the total mass causing the observed motions. We address the first issue by using new measurements of the mass-to-light ratio profile from stellar population constraints that include a radially varying initial mass function. To mitigate the mass–anisotropy degeneracy, we make use of multiple kinematic tracers, including two subpopulations of globular clusters in addition to the galaxy's field stars. We create a hierarchical Bayesian model that addresses several often-neglected systematic uncertainties, such as the statistical weight given to various data sets and the adopted distance. After sampling the posterior probability distribution with a Markov chain Monte Carlo method, we find evidence for a central cusp with a log slope of $\gamma = 1.0^{+0.2}_{-0.4}(\text{stat})^{+0.3}_{-0.5}(\text{sys})$, with the quantified systematic uncertainty dominated by choice of anisotropy profile. This is lower than expected for dark matter halos that have undergone adiabatic contraction, supporting inferences from gravitational lensing that some process has suppressed the steepening of halos in massive galaxies. We also confirm radially biased orbits for the metal-rich globular clusters and tangentially biased orbits for the metal-poor globular clusters, which remains a puzzling finding for an accretion-dominated halo.

Key words: galaxies: elliptical and lenticular, cD – galaxies: halos – galaxies: individual (NGC 1407) – galaxies: kinematics and dynamics

1. Introduction

The concordance cosmological model of dark energy plus cold dark matter (ΛCDM) has had numerous successes in describing the large-scale structure of the universe. The story on the scale of galaxy formation has been more complicated, with discrepancies in the number of satellite galaxies expected around the Milky Way (Klypin et al. 1999; Moore et al. 1999), the masses of the Milky Way satellites that are observed (Boylan-Kolchin et al. 2011; Bullock & Boylan-Kolchin 2017), and the inner slope of the dark matter (DM) density profile of galaxies (Flores & Primack 1994). It is this last point that we focus on here.

Navarro et al. (1997) introduced a double power law model (hereafter the NFW model) of the halo density profile with $\rho \propto r^{-1}$ in the inner regions and $\rho \propto r^{-3}$ in the outer regions, which they found to describe well the form of halos from *N*-body simulations. This model can be generalized to include a variable inner slope, γ, and is often parameterized as

$$\rho(r) = \rho_s \left(\frac{r}{r_s}\right)^{-\gamma} \left(1 + \frac{r}{r_s}\right)^{\gamma - 3}, \quad (1)$$

where r_s is the scale radius that determines where the change in density slope occurs.

For $\gamma = 1$, this corresponds to the original NFW profile.[8] While this "universal" profile provided a good match to their DM-only simulations, deviations from this profile have been observed in various mass regimes. For instance, dwarf galaxies have often been found to have shallower inner density slopes (Simon et al. 2003; Spekkens et al. 2005; Oh et al. 2011; Walker & Peñarrubia 2011, though see Adams et al. 2014; Pineda et al. 2017). On the opposite end of the mass spectrum, Newman et al. (2013b) used both gravitational lensing and stellar dynamics to measure $\langle \gamma \rangle \sim 0.5$ for a sample of massive galaxy clusters.

If DM halos start with an NFW-like steep inner profile, then some physical mechanism for transferring energy to DM in the inner regions is necessary to create the shallower DM profiles observed for some galaxies. Self-interacting or fuzzy DM scenarios have been proposed to solve this issue (e.g., Rocha et al. 2013; Robles et al. 2015; Di Cintio et al. 2017). However, baryonic effects may also explain DM cores, either from bursty star formation at the low-mass end (Navarro et al. 1996; Mashchenko et al. 2008; Pontzen & Governato 2012) or from dynamical friction during gas-poor mergers at the high-mass end (El-Zant et al. 2004). In addition, Dekel et al. (2003) argued that merging satellites whose halos have DM cores

---

[8] In this work, we use the convention $\gamma = -d \log \rho / d \log r$, such that a larger value of γ implies a steeper slope.

would be disrupted outside of the central halo's core, leading to a stable DM core in the central galaxy. Whatever processes are responsible for flattening the DM density profile must compete with the effects of adiabatic contraction (Blumenthal et al. 1986), whereby the infalling of gas during the process of galaxy formation causes a steepening of the halo density profile.

To disentangle these many effects on the halo, we need to observationally map out how the inner DM slope changes as a function of halo mass across a wide range of mass regimes. While there are already many good constraints on this relation for dwarf galaxies and for clusters of galaxies, there remains a dearth of observational measurements of the inner DM slope for halos between the masses of 10^{12} and $10^{13} M_\odot$, which typically host massive early-type galaxies (ETGs). These massive galaxies are particularly critical tests for the presence of new, non-CDM physics, as many of the baryonic effects on the halo are small compared to those for dwarf galaxies.

Mass inferences with dispersion-dominated dynamics suffer from a number of challenges. For one, the total mass is degenerate with the distribution of the orbits of the kinematic tracers being modeled. A general strategy for dealing with this mass–anisotropy degeneracy is to simultaneously model multiple kinematic tracers with separate distributions of their orbits.

Walker & Peñarrubia (2011) applied this approach to the Fornax and Sculptor dwarf spheroidal (dSph) galaxies by splitting their resolved stellar kinematic data into chemo-dynamically distinct components, then making separate mass estimates using each subpopulation. Previous studies of massive ETGs modeled multiple tracer populations such as globular clusters (GCs), planetary nebulae (PNe), and inte-grated-light stellar kinematics to alleviate the mass–anisotropy degeneracy (Schuberth et al. 2010; Agnello et al. 2014; Pota et al. 2015; Oldham & Auger 2016; Zhu et al. 2016).

These studies were able to provide good constraints on the total mass of DM halos, but inferring the detailed density distribution of halos requires a precise determination of the stellar mass distribution. In contrast to the dSph galaxies studied by Walker & Peñarrubia (2011), the inner regions of ETGs are dynamically dominated by baryonic matter. As Pota et al. (2015) found, the degeneracy between the inferred stellar mass-to-light ratio (Υ_*) and the inner DM density slope undermines attempts to draw robust conclusions about the slope of the DM halo. Furthermore, in all of the studies cited above, Υ_* was assumed to be constant across all galactocentric radii (but see Li et al. 2017; Mitzkus et al. 2017; Poci et al. 2017; Oldham & Auger 2018 for work that relaxes this assumption). Given that many ETGs are found to have spatially varying stellar populations, the constant Υ_* assumption is an important systematic uncertainty in understanding the inner DM density distribution (Martín-Navarro et al. 2015; McCon-nell et al. 2016; van Dokkum et al. 2017).

Using data from the SAGES Legacy Unifying Globulars and GalaxieS (SLUGGS) survey[9] (Brodie et al. 2014), we model the dynamics of the massive elliptical galaxy NGC 1407. SLUGGS is a survey of 25 nearby ETGs across a variety of masses, environments, and morphologies. NGC 1407 has been studied by numerous authors (e.g., Romanowsky et al. 2009; Su et al. 2014; Pota et al. 2015), but here we revisit the galaxy

---

9 http://sluggs.ucolick.org

with state-of-the-art stellar population synthesis results, a new method for modeling the stellar mass distribution, and a more rigorous statistical treatment of the influence of multiple disparate data sets. This paper is a pilot work for an expanded study of a larger subset of SLUGGS galaxies.

In Section 2, we summarize the observational data. In Section 3, we describe the dynamical modeling and our method for combining distinct observational constraints. In Section 4, we present the results of applying our model to NGC 1407. In Section 5, we interpret these results in the context of other observations and theoretical predictions. We summarize our findings in Section 6, and we present our full posterior probability distributions in Appendix A. We show the result of various systematic uncertainty tests in Appendix B.

2. Data

NGC 1407 is a bright ($M_K = -25.46$; Jarrett et al. 2000), X-ray luminous ($L_X = 8.6 \times 10^{40}$ erg s^{-1} within $2 R_e$; Su & Irwin 2013), massive elliptical galaxy at the center of its eponymous galaxy group. Brough et al. (2006) argued that on the basis of its high X-ray luminosity and low spiral fraction that the NGC 1407 group is dynamically mature. The central galaxy is a slow rotator ($\lambda_{R_e} = 0.09$; Bellstedt et al. 2017). We adopt a systemic velocity of 1779 km s^{-1} (Quintana et al. 1994). The galaxy shows slight ellipticity (de Vaucouleurs et al. 1991 reported a flattening of $\epsilon = 0.07$), and so we calculate the projected galactocentric radius as

$$ R^2 = q\Delta x^2 + q^{-1}\Delta y^2, \tag{2} $$

where Δx and Δy are coordinate offsets along the major and minor axes, respectively, and q is the axial ratio (b/a). Here we have adopted a position angle of $58\overset{\circ}{.}4$ (Spolaor et al. 2008).

There are numerous conflicting redshift-independent dis-tances for NGC 1407 in the literature. Cantiello et al. (2005) used surface brightness fluctuation (SBF) measurements to obtain a value of 25.1 ± 1.2 Mpc, while Forbes et al. (2006) used the GC luminosity function to obtain a value of 21.2 ± 0.9 Mpc. Using a weighted average of both SBFs and fits to the fundamental plane, Tully et al. (2013) derived a distance of 28.2 ± 3.4 Mpc. Using the Planck Collaboration et al. (2016) cosmological parameters and correcting the recession velocity to the Virgo infall frame, the galaxy has a luminosity distance of 24.2 ± 1.7 Mpc. When including the distance to the galaxy as a free parameter, we use a Gaussian prior with a mean of 26 Mpc and a standard deviation of 2 Mpc. We find an a posteriori distance of $21.0^{+1.5}_{-1.4}$ Mpc (see Section 4) corresponding to a distance scale of 0.102 kpc per arcsecond. It is this distance that we adopt for any distance-dependent results that are not already marginalized over this parameter. We report the effects of adopting a wide uniform prior on the distance in Appendix B.1.

Here we summarize the kinematic, photometric, and stellar population data that we use for our models.

2.1. Stellar Density

We use the same surface brightness profile as Pota et al. (2013), who combined *Subaru*/Suprime-Cam *g* band and *HST*/ACS F435 imaging into a single *B* band profile out to 440″. Masking out the core at $R < 2″$, they fitted a single
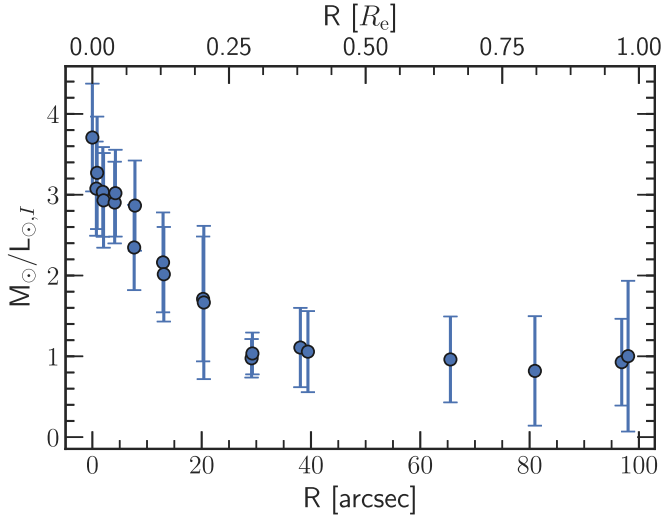
Figure 1. Stellar mass-to-light profile of NGC 1407 from van Dokkum et al. (2017).

Figure 2. Stellar mass surface density. Blue circles show the measured values using the variable Υ_* profile. The blue dashed line shows the best-fit model (see Section 3) of the surface density, with the width of the curve showing the inner 68% of samples. We compare this with a profile derived from a constant Υ_*, shown as the yellow squares. The uncertainties on these points are taken from the typical uncertainties on Υ_*.

Sérsic component (Equation (3)).

$$I(R) = I_0 \exp\left(-b_n \left(\frac{R}{R_e}\right)^{1/n}\right). \qquad (3)$$

Here, I_0 is the central surface density, R_e is the effective radius, n is the Sérsic index, and b_n is a function of n chosen such that $2 L(R_e) = L_{tot}$ (see Equation (18) in Ciotti & Bertin 1999, for an asymptotic expansion of b_n). Pota et al. (2013) found an effective radius of $R_e = 100'' \pm 3''$, a Sérsic index of $n = 4.67 \pm 0.15$, and a central surface brightness of $I_0 = 1.55 \times 10^{11} L_{\odot,B} \, kpc^{-2}$ (adopting a solar absolute magnitude of $M_{\odot,B} = 5.48$).

To derive a stellar mass surface density profile, we use the spatially resolved Υ_* measurements of van Dokkum et al. (2017), shown in Figure 1. Details of the Low Resolution Imaging Spectrograph observations, data reduction, and modeling can be found in Sections 2 and 3 of van Dokkum et al. (2017). Fitting of the extracted 1D spectra was performed with the stellar population synthesis models of Conroy et al. (2018) (an update to those of Conroy & van Dokkum 2012), using the extended stellar library of Villaume et al. (2017) and the MESA Isochrones and Stellar Tracks (MIST) (Choi et al. 2016). The logarithmic slope of the initial mass function (IMF) was allowed to vary in the ranges of $0.08 < M/M_\odot < 0.5$ and $0.5 < M/M_\odot < 1$. For $M/M_\odot > 1$, a Salpeter (1955) log slope of -2.35 was adopted.

Since these Υ_* values were computed for the I band, we use the B–I color profile measured by Spolaor et al. (2008) to convert to a B band Υ_*. We then multiply these Υ_* measurements by the stellar surface brightness profile to obtain the mass surface density profile shown in Figure 2, propagating uncertainties under the assumption that the Υ_* uncertainties dominate over the photometric uncertainties. We compare this variable Υ_* density profile with one determined from multiplying the surface brightness profile by a constant $\Upsilon_* = 8.61$ (chosen to match the two enclosed stellar mass values at $100''$). We see that the variable Υ_* profile is noticeably more compact than the constant Υ_* profile. We discuss this more in Section 5.3.

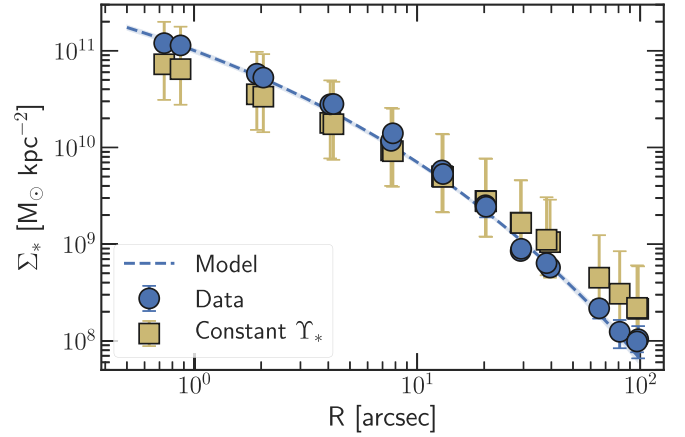The Sérsic fits to the stellar luminosity and mass surface density profiles are listed in Table 1.

Table 1
Sérsic Profile Parameters

	I_0	R_e	n
Stellar luminosity	1.55×10^{11}	100 ± 3	4.67 ± 0.15
Stellar mass	3.25×10^{12}	23 ± 2	3.93 ± 0.05
Red GCs	354	169 ± 7	1.6 ± 0.2
Blue GCs	124	346 ± 30	1.6 ± 0.2

Note. Left to right: central surface density, effective radius (in arcseconds), and Sérsic index. The central surface density has units of $L_{\odot,B} \, kpc^{-2}$ for the stellar luminosity, $M_\odot \, kpc^{-2}$ for the stellar mass, and count $arcmin^{-2}$ for the GCs.

2.2. GC Density

Nearly all massive ETGs have been found to have GC systems with a bimodal color distribution (Brodie & Strader 2006), and NGC 1407 is no exception (Forbes et al. 2006). The red and blue modes are expected to trace metal-rich and metal-poor GCs, respectively, with the basic galaxy formation scenario associating metal-rich GCs with in situ star formation and metal-poor GCs with accretion (Brodie & Strader 2006; Peng et al. 2006; Harris et al. 2017).

Since we model the dynamics of the blue and red GC subpopulations simultaneously, we use separate surface number density profiles for each subpopulation, using the results from Pota et al. (2013). With Subaru/Suprime-Cam g and i band imaging, they fitted a single Sérsic profile plus uniform background contamination model to both the red and blue subpopulations, splitting the two subpopulations at a color of $g - i = 0.98 \, mag$. Their resulting Sérsic parameters are listed in Table 1, and the profiles are shown in Figure 3.

Relative to the field star density distribution, the GC profiles show flatter inner cores, possibly due to tidal destruction of GCs at small galactocentric radii. The red GC subpopulation is more compact than the blue GCs, though both are far more spatially extended than the field stars.

In Figure 4 we show the log slopes of the tracer surface density profiles as a function of radius. The density slope of the red GC subpopulation qualitatively matches that of the field stars in the outer halo, matching expectations that the
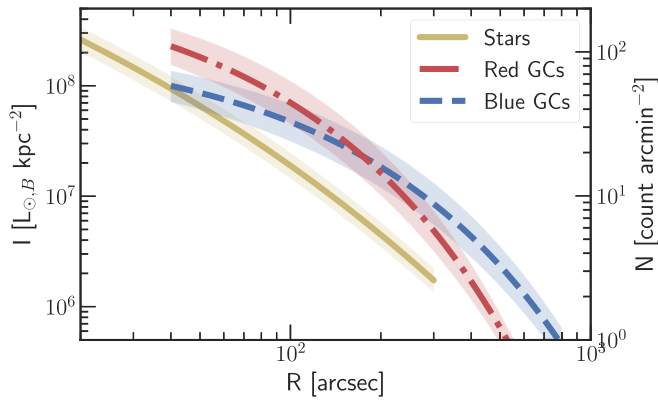
Figure 3. Surface brightness and surface number density profiles for the field stars, blue GCs, and red GCs. The extent of the radial ranges represent where the profiles were fitted to the photometric data, and the width of the curve shows the propagated uncertainty in the Sérsic parameters.
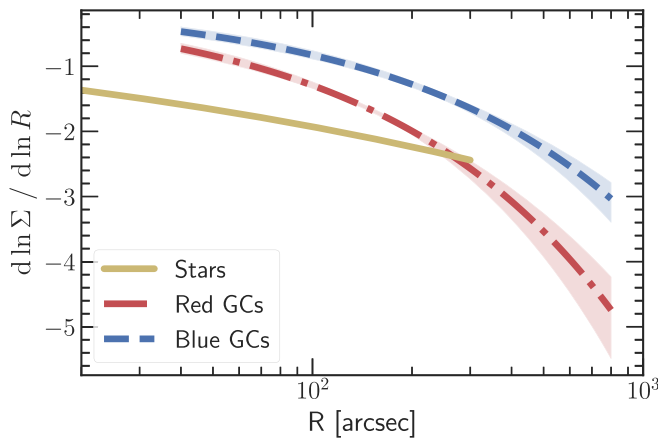

Figure 4. Log slopes of the surface brightness and surface number density profiles for the field stars, blue GCs, and red GCs. The extent of the radial ranges represent where the profiles were fitted to the photometric data, and the width of the curve shows the propagated uncertainty in the Sérsic parameters.

metal-rich GCs are associated with the field star population (Forbes et al. 2012).

2.3. Stellar Kinematics

In the inner $\sim 40''$ ($0.4\,R_e$) of the galaxy, we use longslit spectroscopy along the major axis from the ESO Faint Object Spectrograph and Camera, originally analyzed by Spolaor et al. (2008). These data were re-analyzed by Proctor et al. (2009), who used penalized pixel fitting (Cappellari & Emsellem 2004) to calculate a velocity dispersion profile for the galaxy.

Here we define the velocity dispersion as the root mean square (rms) velocity, $v_{rms} = \sqrt{\langle v^2 \rangle}$. For the longslit data along the major axis, we account for the slight rotational motion by calculating v_{rms} as

$$v_{rms} = \sqrt{\frac{v_{rot}^2}{2} + \sigma^2} \qquad (4)$$

where σ is the standard deviation of the line-of-sight velocity distribution (LOSVD) (Napolitano et al. 2009). With $\langle v/\sigma \rangle \sim 0.09$, there is a difference of less than 3 km s^{-1} between the σ and v_{rms} profiles.
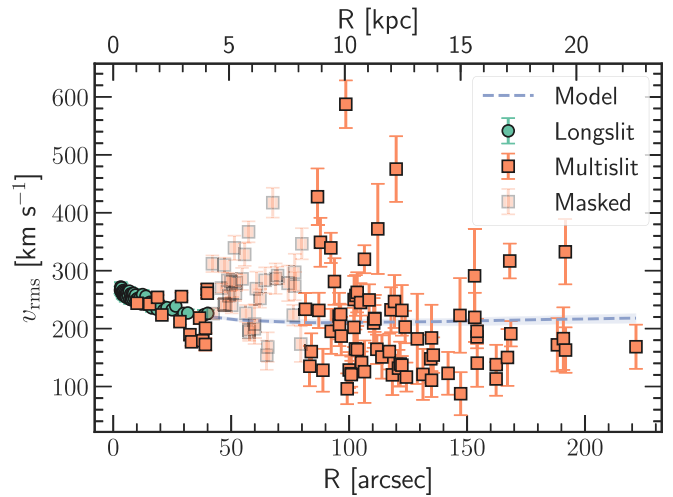

Figure 5. Stellar velocity dispersion data out to $2\,R_e$ (~ 20 kpc). The lighter points between $40''$ and $80''$ show where we mask data due to substructure. The green circles show the longslit data, the orange squares show the multislit data, and the blue line shows the best-fit stellar velocity dispersion model described in Section 3, with the width of the curve showing the inner 68% of samples. We note that the error bars have *not* been visually scaled following the best-fit weighting parameter (Section 3.2).

To reach out to much farther galactocentric radii, we use the Keck/DEIMOS multislit observations presented by Arnold et al. (2014) and Foster et al. (2016), which sample the stellar light in 2D. Using only spectra visually classified as "good" by Foster et al. (2016), these stellar velocity dispersion measurements reach out to $\sim 200''$ ($2\,R_e$), though of course with sparser spatial sampling than the longslit kinematic data. We calculate the velocity dispersion for these 2D measurements as

$$v_{rms} = \sqrt{v_{rot}^2 + \sigma^2}. \qquad (5)$$

These stellar kinematic measurements are shown in Figure 5.

There are two complications in preprocessing the stellar kinematic data. The first is the potential presence of substructure in the kinematics in the region between $40''$ and $80''$. This deviation from a monotonically decreasing velocity dispersion profile was also seen in the velocity dispersion profile measured by van Dokkum et al. (2017), and it is further mirrored in the metallicity bump seen by Pastorello et al. (2014). Following Pota et al. (2015), we mask out this region for our analysis (the lighter points in Figure 5). We discuss the effects of removing these data in Appendix B.2. The second complication is the influence of the central supermassive black hole (SMBH). Rusli et al. (2013) inferred the presence of a $\sim 4 \times 10^9\,M_\odot$ SMBH in NGC 1407 with a corresponding sphere of influence with radius $\sim 2''$. To avoid having to model the dynamical effects of the SMBH, we restrict our analysis to radii outside of $3''$.

2.4. GC Kinematics and Colors

We use the GC kinematics presented in Pota et al. (2015). The spectra for these measurements were obtained from ten Keck/DEIMOS slitmasks. The red and blue GC radial velocities (RVs) in Figure 6 reveal that the two subpopulations have systematically different velocity dispersions in the outer regions. The GC radial velocity measurements for NGC 1407,
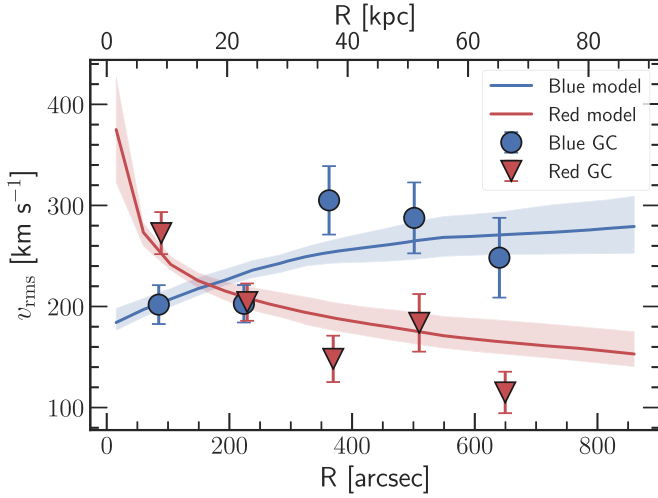
Figure 6. GC velocity dispersion vs. galactocentric radius, with blue GCs and red GCs showing systematically different trends in their scatter at large galactocentric radii. The blue GC subpopulation has a rising velocity dispersion profile, while the red GC subpopulation has a falling velocity dispersion profile. The associated best-fit models of the GC velocity dispersion profiles are described in Section 3, with the width of the curves showing the inner 68% of samples.
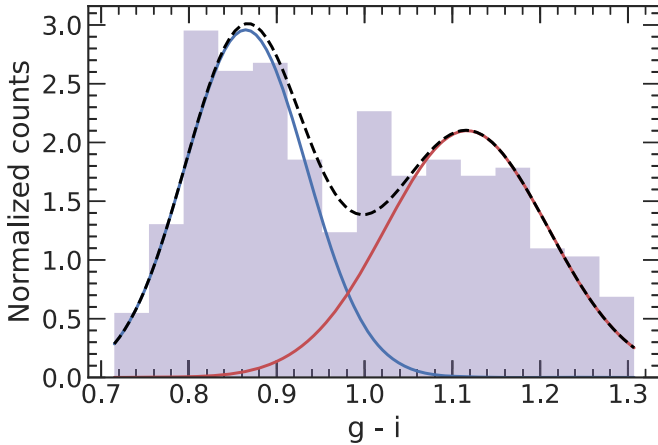

Figure 7. Gaussian mixture model of GC colors from our RV GC data set. The blue and red curves show the Gaussian color distribution for the blue GC and red GC subpopulations, respectively, while the black dashed curve shows that the sum of these distributions accurately captures the observed RV GC color distribution (in the violet histogram).

as well as for the entire SLUGGS sample, can be found in Forbes et al. (2017).

The $g-i$ color distribution of our spectroscopic GC data set, shown in Figure 7, is well matched to the photometric GC catalog presented in Pota et al. (2013). We fit a Gaussian mixture model to the spectroscopic sample color distribution and compare the result with the distributions found for the photometric sample of Pota et al. (2013),[10] listed in Table 2. We find that the color Gaussians of the RV GC sample have nearly identical means to those of the photometric sample, though the blue Gaussian of the RV sample has a slightly larger standard deviation than that of the photometric sample.

We emphasize that we do *not* split the GCs into red and blue subpopulations based on color for the dynamical analysis, but

---

[10] We note that the mean color of the red GCs was swapped with that of NGC 2768 in the presentation of their Table 3.

Table 2
GC Color Gaussian Parameters

	μ_c	σ_c	ϕ
Blue GCs (photometric sample)	0.85	0.05	⋯
Red GCs (photometric sample)	1.10	0.1	⋯
Blue GCs (RV sample)	0.87	0.067	0.52
Red GCs (RV sample)	1.12	0.094	0.48

Note. Comparison of the color distribution of our spectroscopic GC sample with that of the GC system overall. The weights, ϕ, indicate the fraction of GCs which come from the specified subpopulation.

rather use this information to assign a probability of being in either subpopulation for each GC (Section 3.2).

3. Methods

Here we describe the dynamical (Section 3.1) and statistical (Section 3.2) methods that we use to model our data.

3.1. Dynamical Model

Given the low v/σ and near-circular isophotes of the galaxy, we assume spherical symmetry for our model. Further assuming that we have a perfectly collisionless tracer population in steady state, we can write the spherically symmetric Jeans equation as

$$\frac{d(\nu \overline{v_r^2})}{dr} + 2\frac{\beta}{r}\nu \overline{v_r^2} = -\nu\frac{d\Phi}{dr} \quad (6)$$

where ν is the volume density of the tracer, and

$$\beta \equiv 1 - \frac{\sigma_\theta^2 + \sigma_\phi^2}{2\sigma_r^2} \quad (7)$$

is the standard orbital anisotropy parameter (Binney & Tremaine 2008).

We can integrate once to obtain the mean square of the radial component of the velocity, and again to obtain the projected line-of-sight (LOS) rms velocity. Following Mamon & Łokas (2005) the latter is

$$v_{\rm rms,los}^2(R) = \frac{2G}{I(R)}\int_R^\infty K\left(\frac{r}{R}, \beta\right)\nu(r)M(<r)\frac{dr}{r} \quad (8)$$

where $I(R)$ is the surface density profile, $\nu(r)$ is the volume density profile, $M(<r)$ is the enclosed mass profile, and $K(u, \beta)$ is the appropriate Jeans kernel. The Jeans kernel weighs the impact of the orbital anisotropy across the various deprojected radii, r, associated with the projected radius, R.

We note that we only model the LOS $v_{\rm rms}$, and not any higher-order moments of the LOS velocity distribution. If we assume that the anisotropy parameter of a tracer is constant at all radii, then we have

$$K(u, \beta) = \frac{1}{2}u^{2\beta-1}\left[\left(\frac{3}{2} - \beta\right)\sqrt{\pi}\frac{\Gamma(\beta - 1/2)}{\Gamma(\beta)}\right.$$
$$+ \beta B\left(\beta + \frac{1}{2}, \frac{1}{2}; \frac{1}{u^2}\right)$$
$$\left. - B\left(\beta - \frac{1}{2}, \frac{1}{2}; \frac{1}{u^2}\right)\right] \quad (9)$$

where $B(a, b; z)$ is the incomplete Beta function (Mamon & Łokas 2005, Appendix A). By writing the incomplete Beta function in terms of the hypergeometric function,

$$B(a, b; z) = a^{-1} z^a \, _2F_1[a, 1 - b, a + 1; z] \tag{10}$$

we can extend this formula to values of $\beta \leqslant 1/2$, which would otherwise make this expression undefined.

We model our tracer density as a Sérsic profile (Equation (3)). For the blue and red GCs, the parameters of these Sérsic profiles are fixed to the values described in Section 2.2. For the stellar density profile, we freely vary the Sérsic parameters to jointly constrain the stellar surface density profile shown in Section 2.1 and the impact of the stellar mass on the kinematics.

The deprojected volume density profile in the Sérsic model is approximated as

$$\nu(r) = I_0 \frac{b_n^{n(1-p_n)}}{2R_e} \frac{\Gamma(2n)}{\Gamma((3 - p_n)n)}$$
$$\times \left(\frac{r}{R_e}\right)^{-p_n} \exp\left(-b_n \left(\frac{r}{R_e}\right)^{1/n}\right) \tag{11}$$

where the reciprocal polynomial p_n can be found by minimizing the difference with this equation and the density as computed from an inverse Abel transform of the projected surface density (see Equation (19) in Lima Neto et al. 1999 for an appropriate series approximation to p_n).

We use a generalized Navarro-Frenk-White (gNFW) DM density profile of the form given by Equation (1). The enclosed mass profile of this model is found by integrating the spherically symmetric density profile,

$$M_{DM}(<r) = \int_0^r 4\pi r'^2 \rho(r') dr'$$
$$= 4\pi \rho_s \int_0^r r'^2 \left(\frac{r'}{r_s}\right)^{-\gamma} \left(1 + \frac{r'}{r_s}\right)^{\gamma - 3} dr'. \tag{12}$$

Comparing this with the integral form of the hypergeometric function

$$_2F_1[a, b, c; z] = \frac{1}{B(b, c - b)} \int_0^1 x^{b-1}$$
$$\times (1 - x)^{c-b-1}(1 - zx)^{-a} dx \tag{13}$$

where $B(x, y)$ is the complete Beta function, we obtain

$$M_{DM}(<r) = \frac{4\pi \rho_s r_s^3}{\omega} \left(\frac{r}{r_s}\right)^{\omega} {}_2F_1\left[\omega, \omega, \omega + 1; -\frac{r}{r_s}\right] \tag{14}$$

where $\omega \equiv 3 - \gamma$.

The stellar mass is the deprojected enclosed luminosity of the Sérsic density profile, given by

$$M_*(<r) = 2\pi n \Sigma_0 \left(\frac{R_e}{b_n^n}\right)^2 \frac{\Gamma(2n)}{\Gamma((3 - p_n)n)}$$
$$\times \gamma\left[(3 - p_n)n, b_n \left(\frac{r}{R_e}\right)^{1/n}\right] \tag{15}$$

where $\Gamma(z)$ is the complete Gamma function and $\gamma(z, x)$ is the lower incomplete Gamma function (Lima Neto et al. 1999). We

note that here Σ_0 refers to the central surface mass density, not the surface brightness.

The total enclosed mass is thus given by

$$M(<r) = M_{DM}(<r) + M_*(<r) + M_{BH} \tag{16}$$

where we have included the central SMBH (M_{BH}) as a single point mass at $r = 0$.

3.2. Measurement Model

We construct a Bayesian hierarchical model from the previously described dynamical model that is simultaneously constrained by the longslit stellar kinematics, the multislit stellar kinematics, the GC kinematics and colors, and the stellar mass surface density measurements. Since these data cover a range of different observations and modeling assumptions, we use the hyperparameter method of Hobson et al. (2002) to allow the properties of each data set to determine their own relative weights.

For each data set, we assign a parameter, α, that scales the uncertainties on the data set as $\delta x \rightarrow \delta x / \sqrt{\alpha}$. This α parameter can be interpreted as the "trust" in the data set, given the other data available and the model context in which the data are being evaluated. This is similar to the approach adopted by Oldham & Auger (2016) for balancing the contribution of stellar kinematics and GC kinematics to the overall likelihood, though we assign a weight parameter to each data set under consideration. We do not model the covariance between uncertainties in the data sets (see Ma & Berndsen 2014 for an extension of this method to covariant uncertainties).

We note that the introduction of these weight parameters means that we need to take care in specifying the likelihood. For a typical Gaussian likelihood, we can drop the constant $1/\delta x$ uncertainty factor (where δx refers to the measurement uncertainty), as it does not influence our sampling of the posterior distribution. However, the log likelihood for data, x, drawn from a Gaussian of mean, μ, and standard deviation, $\delta x / \sqrt{\alpha}$, would now be

$$\ln \mathcal{L}(x, \delta x) = -\frac{1}{2}\left(\ln\left(\frac{2\pi \delta x^2}{\alpha}\right) + \alpha\left(\frac{x - \mu}{\delta x}\right)^2\right). \tag{17}$$

Thus, there is now a free parameter in the first term that we cannot neglect. The following description of our joint likelihood assumes that all uncertainties on the data have already been weighted as specified here.

For the sake of visual clarity, in this section we write all velocity dispersion quantities as σ, despite the measured velocity dispersions being given by the rms velocity and not the standard deviation of the LOSVD.

We model the stellar velocity dispersion data, $\sigma_i \pm \delta\sigma_i$, as being drawn from a Gaussian distribution about the Jeans model prediction, $\sigma_J(R_i)$.

$$\mathcal{L}_*(\sigma_i, \delta\sigma_i | \sigma_J(R_i)) = \frac{1}{\sqrt{2\pi\delta\sigma_i^2}} \exp\left(-\frac{(\sigma_J(R_i) - \sigma_i)^2}{\delta\sigma_i^2}\right). \tag{18}$$

We treat both the longslit and the multislit data as measuring the same kinematic tracer (and hence σ_J for both is calculated with the same density profile and anisotropy), but we use different weight parameters as discussed above. When separated, we use $\mathcal{L}_{ls}$ and $\mathcal{L}_{ms}$ to refer to the longslit and multislit likelihoods, respectively.

We model the stellar mass surface density data, $\Sigma_i \pm \delta\Sigma_i$, as being drawn from a Gaussian distribution about the proposed Sérsic profile, $\Sigma_m(R_i)$.

$$\mathcal{L}_m(\Sigma_i, \delta\Sigma_i | \Sigma_m(R_i)) = \frac{1}{\sqrt{2\pi\delta\Sigma_i^2}} \exp\left(-\frac{(\Sigma_m(R_i) - \Sigma_i)^2}{\delta\Sigma_i^2}\right).$$

(19)

This is the same Sérsic profile used for the mass modeling, and so while the parameters of this model are primarily constrained by the data presented in Section 2.1, these Sérsic parameters also influence the predicted kinematic data.

Our analysis of the GC kinematic data differs from that of Pota et al. (2015) in that we do not use a strict color cut or bin GC RV measurements by radius. Rather, we follow the approach of Zhu et al. (2016) in modeling GC RVs as a mixture of Gaussians associated with each GC subpopulation. Here the mean velocity is the systemic velocity of the galaxy and the standard deviation is the predicted σ_J from the Jeans model associated with that subpopulation. We model the GC colors as being drawn from the mixture of Gaussians as described in Section 2.4.

Thus, the likelihood for a particular GC measurement (with velocity $v_i \pm \delta v_i$ and $g - i$ color $c_i \pm \delta c_i$), under the assumption that it comes from a particular subpopulation, k, (described by a distinct density profile, anisotropy, and color distribution) is

$$\mathcal{L}_k(v_i, \delta v_i, c_i, \delta c_i | \sigma_{J,k}(R_i))$$

$$= \frac{1}{\sqrt{2\pi(\delta v_i^2 + \sigma_{J,k}^2(R_i))}} \exp\left(-\frac{v_i^2}{\delta v_i^2 + \sigma_{J,k}^2(R_i)}\right)$$

$$\times \frac{1}{\sqrt{2\pi(\delta c_i^2 + \sigma_{c,k}^2)}} \exp\left(-\frac{(c_i - \mu_{c,k})^2}{\delta c_i^2 + \sigma_{c,k}^2}\right)$$

(20)

where $\mu_{c,k}$ and $\sigma_{c,k}$ are the mean and standard deviation of the color Gaussian for the kth subpopulation, and $\sigma_{J,k}$ is the Jeans model prediction.

The likelihood for the GC data is therefore

$$\mathcal{L}_{gc}(v_i, \delta v_i, c_i, \delta c_i) = \sum_{k \in \{b,r\}} \phi_k \mathcal{L}_k(v_i, \delta v_i, c_i, \delta c_i)$$

(21)

where ϕ_k is the mixture model weight for the kth GC subpopulation, satisfying $\sum_k \phi_k = 1$. We note that the probability that an individual GC comes from a particular subpopulation is given by

$$P_k(v, \delta v, c, \delta c) = \frac{\phi_k \mathcal{L}_k(v, \delta v, c, \delta c)}{\sum_j \phi_j \mathcal{L}_j(v, \delta v, c, \delta c)}.$$

(22)

Putting all of the likelihoods together, our final joint likelihood is

$$\mathcal{L} = \prod_i \mathcal{L}_{ls} \times \prod_i \mathcal{L}_{ms} \times \prod_i \mathcal{L}_m \times \prod_i \mathcal{L}_{gc}.$$

(23)

In practice, we compute the log likelihood.

$$\ln \mathcal{L} = \ln \mathcal{L}_{ls} + \ln \mathcal{L}_{ms} + \ln \mathcal{L}_m + \ln \mathcal{L}_{gc}.$$

(24)

Our model has 15 free parameters, listed in Table 3. The parameters are as follows: the scale density of the DM halo (ρ_s), the scale radius of the DM halo (r_s), the inner DM density log slope (γ), the SMBH mass (M_{bh}), the anisotropy of the field

Table 3
Model Parameters

Parameter	Unit	Prior	Fit Value
$\log_{10}\rho_s$	[$M_\odot$ kpc^{-3}]	$\mathcal{U}(3.0, 9.0)$	$6.65^{+0.74}_{-0.99}$
$\log_{10} r_s$	[kpc]	$\mathcal{U}(1.0, 3.0)$	$1.79^{+0.56}_{-0.36}$
γ	[$\cdots$]	$\mathcal{U}(0.0, 2.0)$	$1.06^{+0.22}_{-0.37}$
$\log_{10} M_{bh}$	[$M_\odot$]	$\mathcal{U}(0.0, 11.0)$	$5.11^{+3.11}_{-3.32}$
$\tilde{\beta}_s$	[$\cdots$]	$\mathcal{U}(-1.5, 1.0)$	$-0.31^{+0.08}_{-0.10}$
$\tilde{\beta}_b$	[$\cdots$]	$\mathcal{U}(-1.5, 1.0)$	$-1.08^{+0.32}_{-0.29}$
$\tilde{\beta}_r$	[$\cdots$]	$\mathcal{U}(-1.5, 1.0)$	$0.23^{+0.25}_{-0.24}$
D	[Mpc]	$\mathcal{N}(26.0, 2.0)$	$21.01^{+1.37}_{-1.35}$
$\log_{10}\Sigma_{0,*}$	[$M_\odot$ kpc^{-2}]	$\mathcal{U}(12.0, 13.0)$	$12.53^{+0.05}_{-0.06}$
$\log_{10} R_{eff,*}$	[arcsec]	$\mathcal{U}(1.0, 2.5)$	$1.41^{+0.06}_{-0.05}$
n_*	[$\cdots$]	$\mathcal{U}(1.0, 8.0)$	$4.07^{+0.14}_{-0.13}$
α_{ls}	[$\cdots$]	Exp	$1.89^{+0.47}_{-0.42}$
α_{ms}	[$\cdots$]	Exp	$0.13^{+0.02}_{-0.02}$
α_{gc}	[$\cdots$]	Exp	$1.89^{+1.27}_{-0.80}$
α_{sp}	[$\cdots$]	Exp	$0.36^{+0.15}_{-0.12}$

Note. List of free parameters in our model with their best-fit values. The fit values show the median of the posterior, along with the 68% credible region.

stars (β_s), the anisotropy of the blue GCs (β_b), the anisotropy of the red GCs (β_r), the distance (D), the central stellar mass surface density ($\Sigma_{0,*}$), the stellar mass effective radius (R_e), the stellar mass Sérsic index (n_*), the weight for the longslit data set (α_{ls}), the weight for the multislit data set (α_{ms}), the weight for the GC data set (α_{gc}), and the weight for the stellar mass surface density data set (α_m).

The dynamical model and measurement model was constructed with SLOMO,[11] a Python-based code doing Jeans modeling of spherically symmetric systems. To sample our posterior probability distribution, we use *emcee* (Foreman-Mackey et al. 2013), an implementation of the affine-invariant Markov chain Monte Carlo (MCMC) ensemble sampler described by Goodman & Weare (2010). We run our sampler with 128 walkers for 6000 iterations, rejecting the first 4800 iterations where the chains have not yet fully mixed. The traces of these walkers are shown in Appendix A.

3.3. Parameterizations and Priors

For scale parameters such as ρ_s or r_s, we use a uniform prior over the logarithm of the parameter. For the anisotropy parameters, we re-parameterize to $\tilde{\beta} = -\log_{10}(1 - \beta)$. By adopting a uniform prior over this symmetrized anisotropy parameter, we treat radial and tangential anisotropy values as equally probable. For the distance, we adopt a Gaussian prior as discussed in Section 2. In practice, we truncate this distribution for negative distances. Following Hobson et al. (2002) we adopt an exponential prior over all weight parameters.

3.4. Mock Data Test

After sampling from our posterior distribution, we validate our model by generating a mock data set and performing the same inference as described above on these generated data. We emphasize that, rather than being a test of the appropriateness of our model, this is a test to see how well recoverable is our

---

[11] https://github.com/adwasser/slomo

posterior distribution, given the assumed correctness of our model.

We take the median parameter values from Table 3 to be our "true" parameter values. For each stellar kinematic data set, we use our dynamical model to generate new velocity dispersion values at each radial sample. We sample from a Gaussian with a standard deviation taken from the associated uncertainties in the original data at the respective radial points to generate the mock stellar kinematic data. We generate mock stellar mass surface density measurements analogously.

For the GC data set, we create a blue GC and red GC data set by sampling from the respective model at each radial point for which we have data. We then assign each radial point to either be from the blue or the red subpopulation by comparing a draw from the standard uniform distribution with the ϕ_b value (from Table 2) in our model.

When generating each data set, we scale the standard deviation by the respective best-fit weight values (the α hyperparameters from Table 3). The input uncertainties to the mock model are the same as those in the original data.

3.5. Caveats

Before presenting our results, we discuss a number of caveats to our work. We leave the relaxation of these assumptions for future work.

We have explicitly assumed that NGC 1407 has a spherically symmetric halo and stellar mass distribution. Wet major merger remnants can produce triaxial halos, with the expectation that the stars end up in an oblate spheroid with its minor axis perpendicular to the major axis of its prolate DM halo (Novak et al. 2006). However, NGC 1407 likely built up its halo through many minor mergers, and if the distribution of incoming merger orbits was largely isotropic as could be expected in a group environment, the galaxy could be expected to have a more spherical halo.

The Jeans equations assume that the tracers of the potential are in equilibrium. This requirement will be violated if there are recently accreted tracers or if the relaxation time is relatively short. For the GCs in the outer halo, the long crossing times (on the order of 0.1–1 Gyr) ensure that the relaxation time is long, but mean that any recently accreted GCs will take a long time to phase mix. While there is not any blatantly obvious substructure in the GC kinematic data, a quantitative description of substructure in the tracer population would require a more rigorous determination of the completeness of our kinematic sample.

Since most of the stellar mass (and hence GCs) of the halo was built up by $z \sim 0.1$ (Buitrago et al. 2017, see also Rodriguez-Gomez et al. 2016), this would give GCs accreted prior to this point several crossing times to come into equilibrium. Efforts at quantifying the effect of nonequilibrium tracers on the mass profiles inferred from spherical Jeans modeling have found a systematic uncertainty on the order of 10%–25% (Kafle et al. 2018; Wang et al. 2018).

We assume that the LOSVD is intrinsically Gaussian. More detailed models (e.g., Romanowsky & Kochanek 2001; Napolitano et al. 2014) would be necessary to make use of higher-order moments of the LOSVD.

Another major assumption we make is that the orbital anisotropies of our tracers are constant with radius. Generically, we would expect the anisotropy to take on different values at different distances from the center of the galaxy (e.g.,
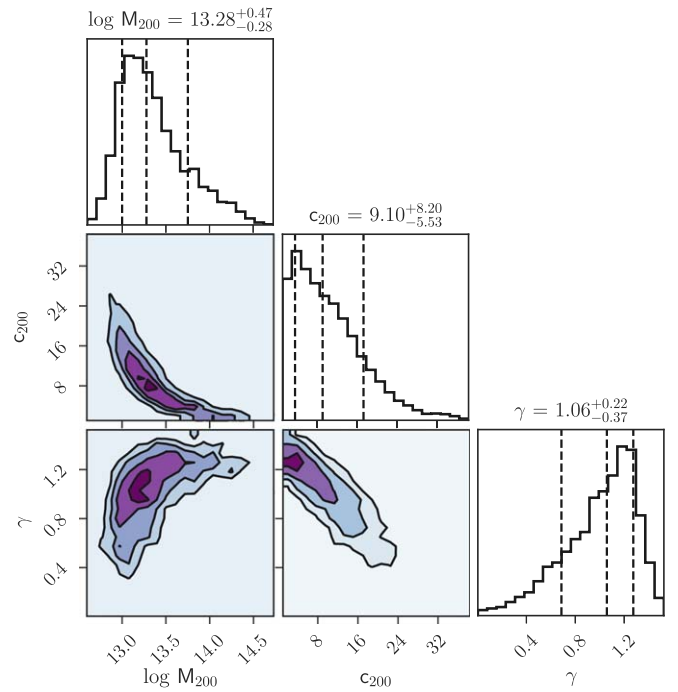

Figure 8. Posterior distribution of halo parameters. Histograms along the diagonal show the marginalized posterior distributions of the halo mass (in $M_\odot$), halo concentration, and halo inner density slope. The dashed vertical lines mark the 16th, 50th, and 84th percentiles. The contours (at levels equivalent to 0.5, 1, 1.5, and 2σ for a 2D Gaussian distribution) show the covariances between these parameters. We note the strong degeneracy among all three halo parameters.

Xu et al. 2017). There are a multitude of ways of parameterizing this anisotropy profile, including that presented by Merritt (1985) and that preferred by Mamon & Łokas (2005). However, given both the diversity of anisotropy profiles seen in simulated galaxies and the complexity evident in the Milky Way stellar anisotropy profile (e.g., Kafle et al. 2012), we opt for a simpler model that can be easily marginalized over. We show the result of modeling constant-β profiles given mock data generated with varying-β profiles in Appendix B.3. This anisotropy assumption contributes the largest systemic uncertainty to the mass inference, and thus motivates the future study of orbital anisotropy in the outer stellar halos of galaxies.

To the extent that we expect any cores created in DM halos to have their own spatial scale independent of the scale radius of the halo, a more robust test to distinguish between a DM cusp and a core should treat these two radii separately. For instance, one can allow for a DM core out to some r_{core}, then have $\rho \propto r^{-1}$ between that core radius and the scale radius, r_s, then transition to having $\rho \propto r^{-3}$ as in a standard NFW halo.

We only have direct constraints on the stellar mass-to-light ratio, Υ_*, in the region studied by van Dokkum et al. (2017), within $100''$. The stellar mass inferred for the outer regions of the galaxy is thus extrapolated from the Sérsic model that best fits the data in the inner region. We show a comparison inference for a radially invariant Υ_* model in Appendix B.4.

4. Results

We show the full posterior distribution in Appendix A. We show the DM halo parameters in Figure 8, where we have converted the halo parameters of ρ_s and r_s to the virial halo
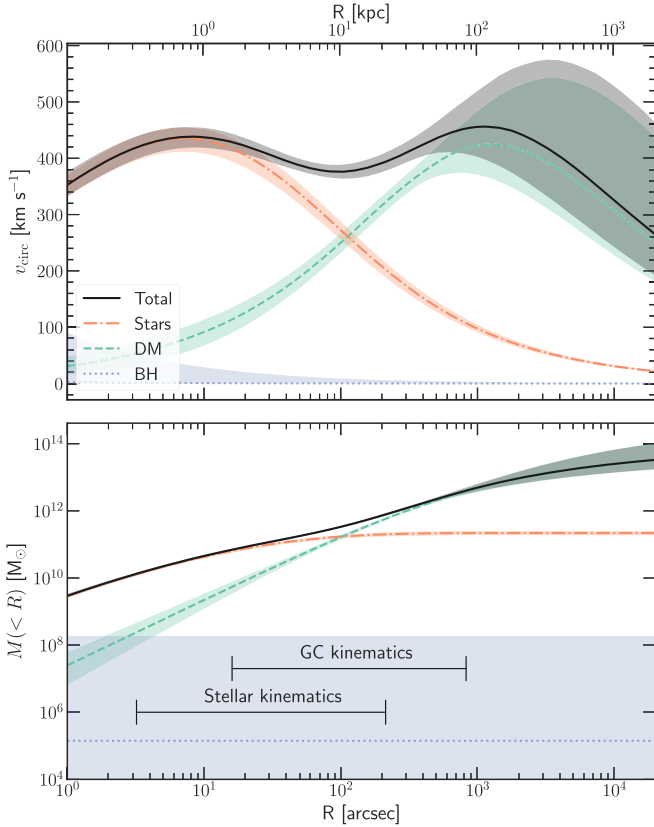
Figure 9. Top: circular velocity profiles of the mass components of the best-fit model, with the width of the curve showing the central 68% of samples. Bottom: same, but showing the enclosed mass of each component. The horizontal bars indicate where we have constraints from stellar and GC kinematics.

Table 4
Derived Parameters

	Unit	Value
$\log_{10} M_{200}$	$[M_\odot]$	$13.3^{+0.5}_{-0.3}$
c_{200}	$[\cdots]$	9^{+8}_{-6}
r_{200}	[kpc]	560^{+250}_{-110}
$\log_{10} M_*$	$[M_\odot]$	$11.34^{+0.06}_{-0.07}$
$f_{\rm DM}$	$[\cdots]$	$0.91^{+0.01}_{-0.01}$

Note. List of quantities derived from free parameters. γ is listed in Table 3.

mass and concentration. We use the convention of defining the virial mass as the enclosed mass with an average density 200 times that of the critical density of the universe at $z = 0$.

$$M_{200} \equiv M(<r_{200}) = \frac{4\pi}{3} r_{200}^3 (200\rho_{\rm crit}). \quad (25)$$

The halo concentration is then defined as $c_{200} \equiv r_{200}/r_s$. For the Planck Collaboration et al. (2016) cosmological parameters, the critical density is $\rho_{\rm crit}(z = 0) = 127.58\ M_\odot\ {\rm kpc}^{-3}$. These halo parameters, along with other derived quantities, are reported in Table 4. We find strong evidence for a DM cusp in NGC 1407, with $\gamma = 1.0^{+0.2}_{-0.4}$. The posterior distribution has 92.9% of samples with $\gamma > 0.5$, disfavoring a cored-NFW profile.
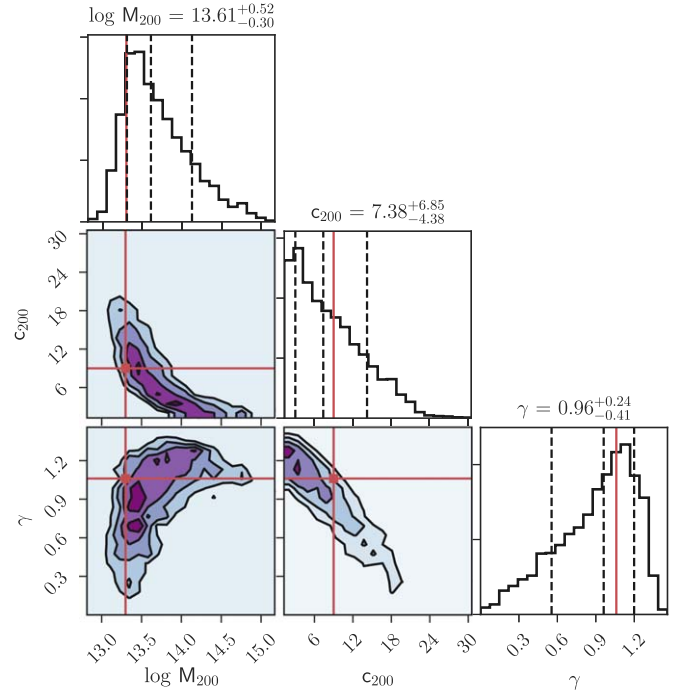
Figure 10. Posterior probability distribution from modeling our mock data set. Red solid lines show the model parameters used to generate the data set.

Our best-fitting model predictions are shown along with the corresponding data for the stellar kinematics in Figure 5, for the GC kinematics in Figure 6, and for the stellar mass surface density in Figure 2.

We show the decomposition of the enclosed mass profile into stellar, DM, and BH components in Figure 9. Here we see that the overlap in the spatial regions probed by the GC and stellar kinematic data cover the crucial region where the DM halo becomes gravitationally dominant over the stellar mass. As anticipated, we have weak constraints on the mass of the central SMBH, which we have treated as a nuisance parameter in the modeling.

4.1. Mock Data Test Results

Our inference on the mock data shows that most of the parameters used to generate the mock data are well recovered. We show the recovery of our input halo model parameters in Figure 10, and we show the full parameter set in Figure 19 in Appendix A . We find excellent recovery of the halo mass parameters. However, our recovery of the stellar anisotropy is biased toward more tangential orbits.

Since these mock data were generated using the model that was used for fitting, the successful recovery merely validates our statistical uncertainties; we defer an in-depth discussion of the systematic uncertainties of our modeling assumptions to Appendix B. The largest quantified source of systematic uncertainty in the halo inner density slope is from the choice of anisotropy profile, which lowers γ by ~ 0.5.

4.2. Literature Comparisons for NGC 1407

In this section, we compare our mass inferences with those from some recent observational studies. We compare both the DM fraction,

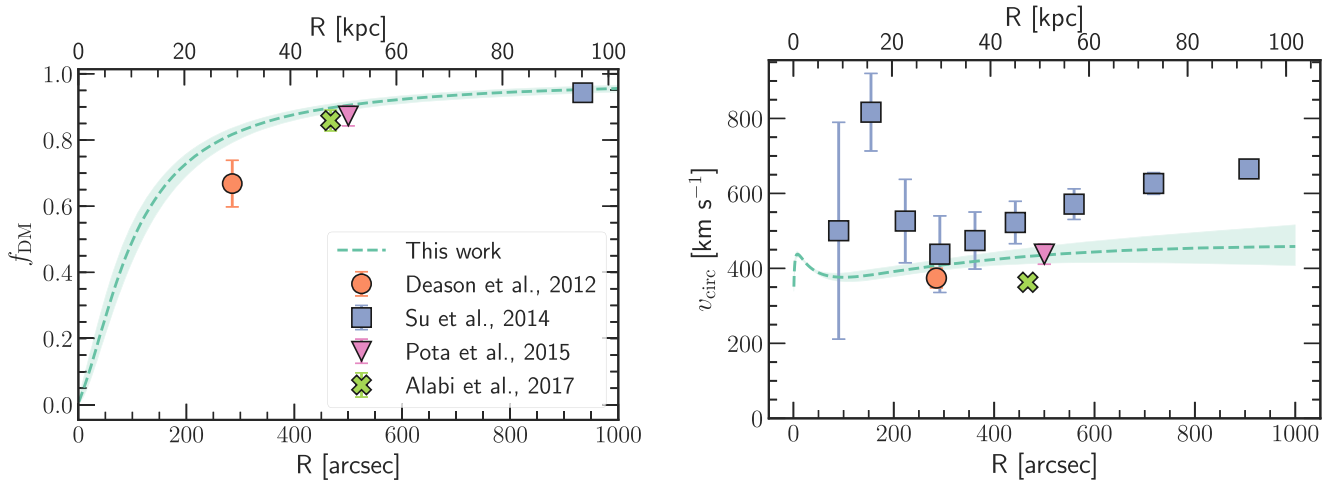$$f_{\rm DM}(<R) = 1 - M_*(<R)/M_{\rm tot}(<R), \quad (26)$$

Figure 11. Left: DM fraction as a function of radius, compared with measurements from the literature. Right: circular velocity as a function of radius, compared with measurements from the literature. The width of the curves indicate the central 68% of samples.

and the circular velocity

$$v_{\mathrm{circ}}(R) = \sqrt{GM/R}. \qquad (27)$$

The DM fractions and circular velocity profiles from Pota et al. (2015), Deason et al. (2012), Su et al. (2014), and Alabi et al. (2017) are compared with our results in Figure 11. These are both quantities that vary with radius, so we plot values at a given angular radius on the sky to make a proper comparison. For the DM fractions, we scale the reported measurements by

$$1 - f_{\mathrm{DM}} \rightarrow \left(\frac{d_{\mathrm{us}}}{d_{\mathrm{them}}}\right)(1 - f_{\mathrm{DM}}) \qquad (28)$$

to account for the differences in their adopted distances. The stellar mass will scale with two factors of the distance for the luminosity distance dependence, and the dynamical mass will scale inversely with one factor of distance, leading to the scaling of the baryon fraction by one factor of the adopted distance.

Our total mass result is consistent with that of Pota et al. (2015), who adopted a distance of 28.05 Mpc. This is to be expected, given that we use a similar data set and modeling technique. They reported $f_{\mathrm{DM}} = 0.83^{+0.04}_{-0.04}$ at 500″, slightly below the value of $0.90^{+0.01}_{-0.02}$ that we find at the same radius.

Deason et al. (2012) used a distribution function–maximum likelihood method to constrain the mass of 15 ETGs using PNe and GCs. They assumed a distance to NGC 1407 of 20.9 Mpc, and they modeled the total mass as a power law. For an assumed Salpeter IMF ($6 < \Upsilon_{*,B} < 10$), they found $f_{\mathrm{DM}} = 0.67 \pm 0.05$ within 285″, whereas we find $f_{\mathrm{DM}} = 0.82^{+0.02}_{-0.03}$.

Su et al. (2014) modeled the X-ray emission of hot gas surrounding NGC 1407. Under the assumption that the gas is in hydrostatic equilibrium, they constrained the total mass profile of the galaxy and decomposed this into stellar, gas, and DM components. They modeled the DM halo using an NFW profile, and assumed a mass-to-light ratio of $\Upsilon_K = 1.17\,M_\odot/L_{\odot,K}$ and a distance of 22.08 Mpc. Within the inner 934″ (100 kpc at their adopted distance), they found $f_{\mathrm{DM}} = 0.94$. We find $f_{\mathrm{DM}} = 0.95^{+0.01}_{-0.01}$ within the same enclosed area.

Alabi et al. (2017) also used GCs as tracers, but applied the tracer mass estimator technique of Watkins et al. (2010) to 32 ETGs, including NGC 1407. They assumed a distance of 26.8 Mpc. They reported results for multiple assumptions for β, and we compare with their result ($f_{\mathrm{DM}} = 0.82 \pm 0.04$ at 60.7 kpc) that assumes an anisotropy of $\beta = 0$ for all the GCs (though we note that their value of f_{DM} only varies by 0.04 between the $\beta = -0.5$ and the $\beta = 0.5$ cases).

We find good agreement in the measured DM fractions shown in Figure 11, though there is a slight offset between our value and that of Deason et al. (2012). Our total mass estimate is largely in agreement with those of other dynamical studies of NGC 1407, though we find that the X-ray mass measurements of Su et al. (2014) are noticeably larger at $R \sim 20$ kpc and also at $R \gtrsim 50$ kpc. This is consistent with other X-ray studies of NGC 1407 (e.g., Zhang et al. 2007; Romanowsky et al. 2009; Das et al. 2010, though see Humphrey et al. 2006), and it suggests systematic differences in the X-ray and the dynamical modeling.

Disagreements between X-ray and dynamical mass measurements have been seen before in numerous studies of ETGs, and are sometimes attributed to hot halo gas being out of hydrostatic equilibrium or supported by nonthermal pressures (Churazov et al. 2010; Shen & Gebhardt 2010). Furthermore, directional gas compression and decompression can cause asymmetric deviations from optically derived mass measurements (Paggi et al. 2017).

4.3. Halo Mass–Concentration and Stellar Mass–Halo Mass Relations

Given that we find a nearly NFW halo, we compare our virial mass and concentration with the M_{200}–c_{200} relation of relaxed NFW halos from Dutton & Macciò (2014). This relation, along with measurements from the literature, are shown in Figure 12. Here we see good agreement between our median DM halo parameters and those expected from the mass–concentration relation.

Figure 13 compares our inference of the halo mass and stellar mass with the M_*–M_{halo} relation from Rodríguez-Puebla et al. (2017). Here we have recalculated our virial mass to match the definition used by Rodríguez-Puebla et al. at $z = 0$, with $h = 0.678$ and $\Delta_{\mathrm{vir}} = 333$. We find that NGC 1407 lies
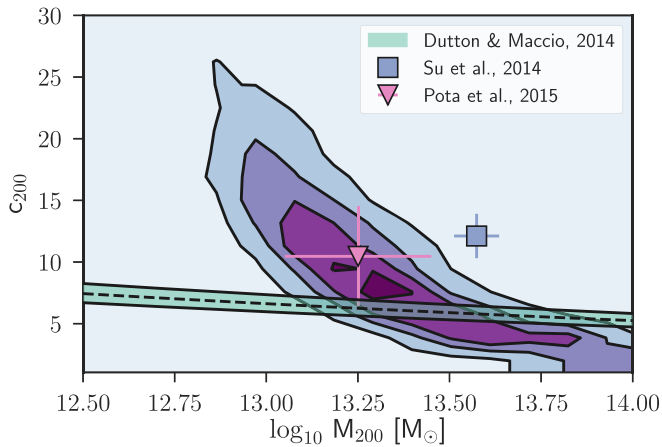
Figure 12. Posterior distribution of halo mass and concentration for NGC 1407 shown in contours. The green line shows the relation from Dutton & Macciò (2014) with characteristic scatter.
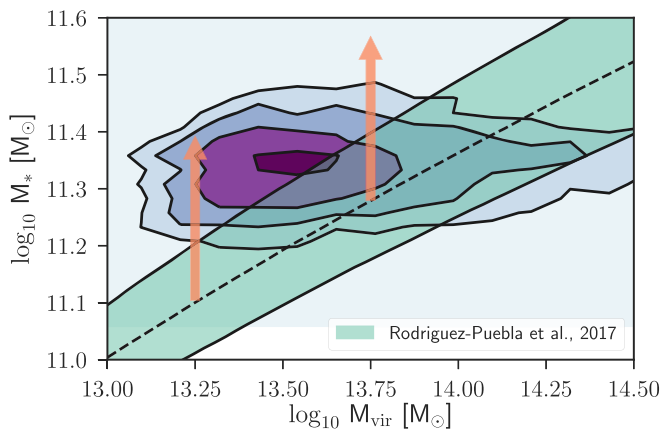

Figure 13. Posterior distribution of stellar mass and halo mass for NGC 1407 shown in contours. The green line shows the stellar mass–halo mass relation from Rodríguez-Puebla et al. (2017) with uncertainties propagated for the 68% credible interval. The orange arrows show the change in stellar mass from a Chabrier (2003) IMF to a Salpeter (1955) IMF, with a resulting shift for the prediction of 0.3 dex.

slightly above the M_*–M_{halo} relation from Rodríguez-Puebla et al. (2017). However, we have indicated the shift in stellar mass that would occur if they had adopted a Salpeter IMF rather than a Chabrier IMF. We see that this Salpeter IMF stellar mass–halo mass relation is consistent with our inference.

4.4. Distance

One unique aspect of this work is that we freely vary the distance, informed by a weak Gaussian prior from previous redshift-independent distance measurements (see Section 2). With the stellar mass-to-light ratio known to a reasonable degree of uncertainty, this becomes a nontrivial systematic uncertainty, as indicated by the covariance of distance with the inner DM density slope, the stellar anisotropy, and the stellar mass distribution parameters shown in the posterior distributions of Appendix A.

We find a distance of $21.0^{+1.4}_{-1.4}$ Mpc. This is a notable offset from our prior distribution on distance, which was a Gaussian with a mean of 26 Mpc and a standard deviation of 2 Mpc. Our result is inconsistent with the Tully et al. (2013) combined SBF/fundamental plane measured distance. However, our

inferred distance is closer to the luminosity distance of 24.2 ± 1.7 Mpc at the observed redshift, and in full agreement with the Forbes et al. (2006) distance constraint from modeling the GC luminosity function. We ran tests fixing the distance to the mean of our prior distribution, and found a lower value of γ, consistent with the negative covariance between the two parameters seen in the posterior distributions shown in Appendix A. Thus to the extent that our adopted distance is considered low (compared to the wide range of literature values), we find a robust upper bound on γ.

4.5. SMBH

Rusli et al. (2013) modeled the stellar kinematics of 10 ETGs to constrain their SMBH masses. For NGC 1407, they found $M_{BH} = 4.5^{+0.9}_{-0.4} \times 10^9 M_{\odot}$. Since we, by design, do not model the detailed dynamics of stellar orbits near the SMBH, we only get weak constraints on its mass. However, our constraints indicate that the SMBH mass of NGC 1407 could be somewhat lower. With a uniform prior for $\log_{10} M_{bh} < 11$, we find that the posterior distribution on M_{bh} cuts off at approximately $2 \times 10^9 M_{\odot}$.

While Rusli et al. (2013) treated the systematics of having a DM halo in their inference of the SMBH mass, they treated the stellar mass as a constant Υ_* times the stellar luminosity profile. NGC 1407 lies slightly above the standard M_{BH}–σ relation, by a factor of approximately 1.5 times the intrinsic scatter (McConnell et al. 2013). It is conceivable that some of the mass inferred for the SMBH is in fact associated with a more bottom-heavy IMF in the center of the galaxy.

McConnell et al. (2013) investigated the effect of radial Υ_* gradients on the inferred masses of SMBHs, finding that a log slope, $d \log \Upsilon_*/d \log r$, which varied from -0.2 to 0.2 had little impact on the inferred M_{bh}. However, the radial variation in Υ_* for NGC 1407 appears to be somewhat steeper, with a log slope of ~ -0.3 (van Dokkum et al. 2017).

5. Discussion

5.1. The γ–M_{halo} Relation

Few measurements have been made of the inner DM density slope for massive ETGs for the reasons discussed in Section 1. Here we discuss both the measurements and predictions for galaxies in this mass regime and for galaxies across a broad range of masses, focusing first on giant elliptical galaxies.

Pota et al. (2015) also modeled NGC 1407 using GC and stellar kinematics, finding $\gamma \sim 0.6$. We attribute the difference between this value and our own inference to be primarily due to our more precise determination of the stellar mass distribution and also to fitting distance as a free parameter. Agnello et al. (2014) modeled the dynamics of the GC system of M87, the Virgo cluster central galaxy. They found that the behavior of the inner DM density profile followed a power law, $\rho \sim r^{-\gamma}$ with $\gamma \approx 1.6$. Oldham & Auger (2016, 2018) also modeled the dynamics of M87, but found evidence for a DM core ($\gamma \lesssim 0.5$). They attributed this difference to their inclusion of central stellar kinematics in the inference, although we also note that they used a less restricted GC spectroscopic sample than Agnello et al. (2014). Zhu et al. (2016) modeled the dynamics of field stars, GCs, and PNe in the massive elliptical galaxy NGC 5846 (based in part on SLUGGS data). They ran models with a fixed DM core and with a fixed DM cusp, finding a preference for the model with the cored halo.
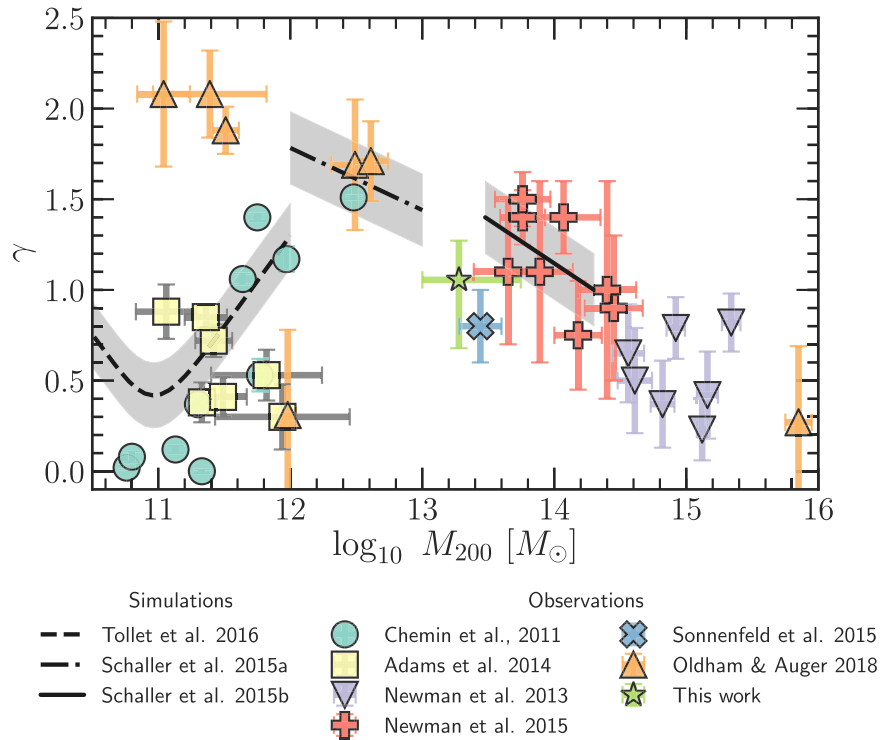
Figure 14. The γ–M_{halo} relation from a wide range of theoretical and observational studies. We see that ΛCDM simulations with hydrodynamics (black lines) largely agree with observations (multi-colored points, described in the text). DM core creation occurs most strongly for $10^{11}\,M_\odot$ halos, with an additional trend toward shallower halos at the highest halo masses. NGC 1407 follows the general trend of steepening density slope with decreasing halo mass, though the median value of γ is slightly below what would have been interpolated from both theory and observation.

Thomas et al. (2007) modeled the stellar dynamics of 17 ETGs in the Coma cluster with both NFW halo models and LOG halo models (which include a central core), though they were unable to distinguish between the two scenarios with the available data. Napolitano et al. (2010) looked at trends of central DM density and radius for a large sample of low-redshift ETGs, finding evidence for an inner DM density log slope of ~1.6, in turn suggesting the need for baryonic processes to contract the halo. While this result is fairly independent of assumptions about the IMF, it is based on stacked galaxy data and thus it cannot be used to provide γ for individual galaxies.

In Figure 14 we show how NGC 1407 compares with the observed and predicted dependence of γ on halo mass. We restrict our observational comparisons in this figure to studies that allowed for a variable inner DM density log slope. We emphasize that due to the varied definitions, methods of inference, and sources of data used to constrain γ, Figure 14 is intended merely as a schematic of what we might expect of DM halos across a wide mass range ($10.5 < \log_{10} M_{200}/M_\odot < 16$).

We summarize the cited observational studies shown in this figure. Chemin et al. (2011) modeled the rotation curves of spiral galaxies with Einasto halos. They reported the log slope of the best-fit Einasto density profile at $\log(r/r_s) = -1.5$, and we compare with their result, which assumes a Kroupa IMF. Adams et al. (2014) modeled the gas and stellar dynamics of dwarf galaxies using both a gNFW profile and a cored Burkert profile. Newman et al. (2013a, 2013b) modeled galaxy clusters and groups with constraints from lensing and stellar dynamics with a gNFW profile, finding halos with both NFW cusps and slightly shallower ($\gamma \sim 0.5$) slopes. Oldham & Auger (2018) modeled strongly lensed ETGs, confirming the decreasing γ

trend at large halo masses. We remove the two systems (J1446 and J1606) for which they find minimal constraints from the lensing data.

The observations of high-mass galaxy clusters suggest a decreasing trend of γ with M_{halo}. NGC 1407 is consistent with this trend, though it may lie on the turnover region that would be necessary to connect to the increasing trend of γ at the low-mass regime. In subsequent work we will check where this turnover happens with a larger sample of galaxies down to lower halo masses.

Simulations that constrain the relation shown in Figure 14 must address physics across a wide range of spatial scales. Tollet et al. (2016) used the NIHAO hydrodynamical cosmological zoom-in simulations to make predictions at $\log M_{200}/M_\odot < 12$. They measured the DM density profiles for their galaxies and reported the log slope in the region between 1% and 2% of the virial radius. Schaller et al. (2015a, 2015b) used the EAGLE simulations to make predictions for higher-mass galaxy clusters. They fitted a gNFW density profile to their halos and reported the inner asymptotic log slope.

We see two emerging trends in the γ–M_{halo} relation. At the range of dwarf and spiral galaxies ($M_{200} \sim 10^{11}$–$10^{12}\,M_\odot$), γ is predicted to increase with halo mass, though there is a large range of observed γ values in the observations. For hydrodynamic simulations in this regime, DM core creation is associated with bursty star formation (Tollet et al. 2016). Thus, this trend can be understood as the energy associated with baryonic feedback becoming less and less significant relative to the depth of the potential associated with the halo. At the range of galaxy groups and clusters ($M_{200} \sim 10^{13}$–$10^{16}\,M_\odot$), there is a decreasing trend of γ with halo mass. This has often
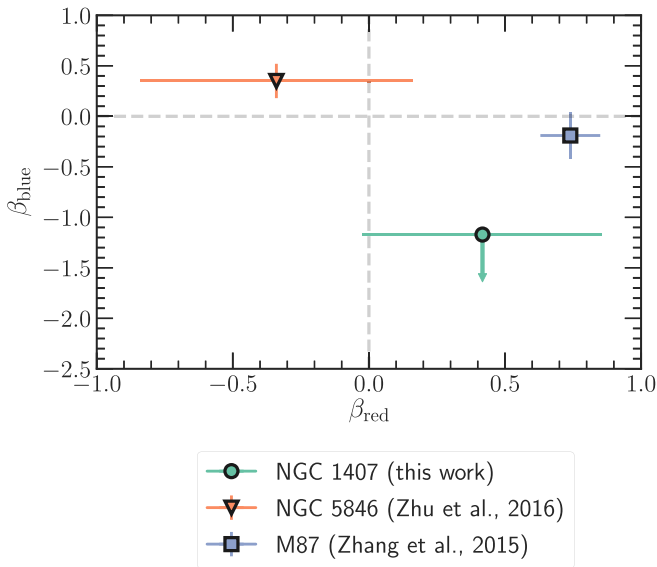
Figure 15. Blue GC orbital anisotropy vs. red GC anisotropy for NGC 1407 compared with those of NGC 5846 (Zhu et al. 2016) and M87 (Zhang et al. 2015). For M87, we show their result at a distance of 100 kpc. Isotropic values of β are indicated by the gray-dashed line.
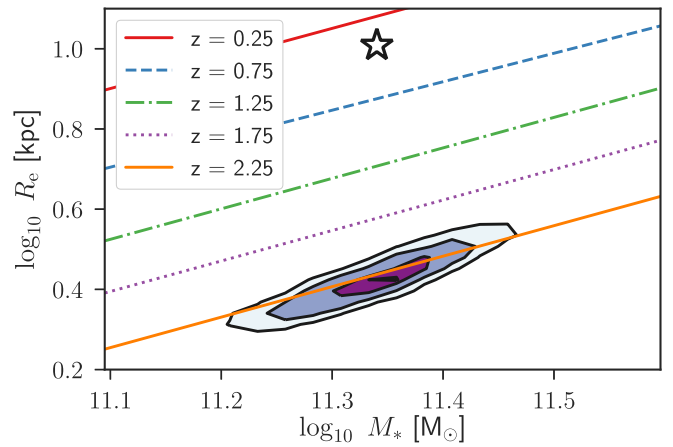

Figure 16. Stellar size–mass relations at different redshifts from van der Wel et al. (2014), compared with our inference for NGC 1407 (purple contours). The B band R_e value of NGC 1407 is indicated by the star.

been interpreted as increased dynamical heating for halos that have experienced more satellite mergers (El-Zant et al. 2004; Laporte & White 2015).

Massive elliptical galaxies like NGC 1407 ought to have the steepest inner density profiles with $\gamma > 1$, owing to the fact that they lie at the intersection of the two competing trends discussed above (i.e., minimal heating from stellar feedback and mergers), and due to the effect of adiabatic contraction (Blumenthal et al. 1986; Gnedin et al. 2004).

We see that our median value for γ falls slightly below the predictions from Schaller et al. (2015a, 2015b) (though consistent within the uncertainty). However, this value is consistent with the results from the analysis of Sonnenfeld et al. (2015), who found an average inner DM density slope of $\gamma = 0.80^{+0.18}_{-0.22}$ for a sample of 81 strongly lensed massive ETGs.

The above discrepancy between theory and observation could be an indication that some mechanism is needed to prevent the steepening of the halo density profile. Self-interacting dark matter (SIDM) could be one such mechanism, as the nonzero collisional cross section allows for heat transfer in the inner regions of the halo. Rocha et al. (2013) compared the structure of self-interacting DM halos with that of standard CDM halos for two cross sections, $\sigma/m = 0.1\,\mathrm{cm}^2\,\mathrm{g}^{-1}$ and $\sigma/m = 1\,\mathrm{cm}^2\,\mathrm{g}^{-1}$. They found that large cross sections lead to DM cores within $\sim$50 kpc. Our result disfavors this large a cross section, though we note that it is difficult to rule out their result for the smaller cross section. In addition, the lack of baryonic physics in these simulations makes a proper comparison difficult.

Di Cintio et al. (2017) used hydrodynamic simulations to explore the effect of SIDM on the baryonic and DM density distributions of Milky Way-mass galaxies. They used a significantly higher cross section, $\sigma/m = 10\,\mathrm{cm}^2\,\mathrm{g}^{-1}$, than Rocha et al. They reported the log slope of the density profiles between 1% and 2% of the virial radius for both standard CDM simulations and SIDM runs and found a decrease of 0.5–0.7 in γ from the standard run to the SIDM one.

Alternatively, feedback from AGNs could be an important mechanism for transferring energy to the central DM (Martizzi et al. 2013; Peirani et al. 2017), analogous to the way that bursty star formation induces potential fluctuations in low-mass galaxies (Pontzen & Governato 2012). Even in absence of any AGN feedback, dry merging of galaxies can slightly decrease the DM density slope, though not enough to fully counteract the effects of adiabatic contraction (Dutton et al. 2015).

Given the paucity of observational constraints and the nontrivial systematic uncertainties in measuring the halo density slope, any connection between our best-fit value of γ and any particular physical cause is largely speculation at this point. However, this ambiguity motivates further work to fill in the remaining observational gaps.

5.2. Halo Anisotropy

The orbital anisotropy of stars and star clusters in the outer stellar halos of galaxies has received much attention in recent years. We find that the blue (metal-poor) GCs have tangentially biased orbits ($\beta_{\mathrm{blue}} \lesssim -4$), while the red (metal-rich) GCs have radially biased orbits ($\beta_{\mathrm{red}} \sim 0.4$).

Dynamical differences between the red and blue GC subpopulations have been seen before. Pota et al. (2013) calculated the kurtosis of the GC LOSVD as a proxy for orbital anisotropy for a sample of 12 ETGs. While they found that the kurtosis values for individual galaxies were largely consistent with isotropic orbits, they found that the blue GCs had, on average, negative kurtosis (suggesting tangential anisotropy) in the outskirts while red GCs had, on average, positive kurtosis (suggesting radial anisotropy) in the outer regions.

Pota et al. (2015) also found tangential blue GCs and radial red GCs for NGC 1407 using Jeans models; we note that we have modeled the same GC data set as the Pota et al. study.

There have been numerous studies of the dynamics of the GC system of M87. Romanowsky & Kochanek (2001) used the Schwarzschild orbit library method to model the GCs and stars. They found that the orbits of the GCs as a whole system were near isotropic at large radii. Zhu et al. (2014) used made-to-measure models to infer the orbits of GCs as a single population, and found orbits that were similarly near isotropic across most of the spatial extent of the galaxy. Agnello et al. (2014) found evidence for three GC subpopulations. For both the bluest and reddest subpopulations they found mildly

tangential orbits at $1 R_e$, while they found the intermediate subpopulation to have slightly radial orbits at the same distance. Zhang et al. (2015) modeled the dynamics of the red and blue GC subpopulations separately using Jeans models. They found slightly tangential ($\beta \sim -0.5$) blue GCs in the inner and outer regions of the galaxy, and radially biased ($\beta \sim 0.5$) red GCs. Oldham & Auger (2016) also modeled blue and red GC subpopulations of M87, finding mildly radially biased orbits for both blue and red GCs. Overall the consensus for halo anisotropy in M87 seems to be that, if red and blue GCs have different orbital anisotropies, the blue GC orbits are somewhat more tangentially biased.

Zhu et al. (2016) used made-to-measure models to constrain the β-profiles of stars, PNe, and GCs in NGC 5846, following up on earlier Jeans modeling work by Napolitano et al. (2014). They found the opposite trend for this galaxy compared with NGC 1407, with tangentially biased or isotropic red GCs and radially biased blue GCs. The PNe trace the field star population in the center and go from radial to marginally tangential orbits out to ∼30 kpc.

We compare some of these studies that separately analyze blue and red GCs in Figure 15. There seems to be a diversity of results, with some studies finding the blue GCs to have more tangential orbits than the red GCs, and others finding the opposite result. However, none of the studies find both red and blue GCs in a single galaxy to have radial orbits (the upper right quadrant of the figure).

This result is puzzling, since the outer stellar halos of galaxies built up by mergers are expected to produce radially biased orbits (e.g., Dekel et al. 2005; Oñorbe et al. 2007; Prieto & Gnedin 2008), and the majority of blue GCs have most likely been brought into the present-day host galaxy via satellite accretions.

Röttgers et al. (2014) used hydrodynamic zoom simulations from Oser et al. (2010) to examine the connection between orbital anisotropy and the fraction of stars formed in situ. They found that accreted stars were more radially biased than in situ stars. To the extent that the blue and red GCs could be expected to trace accreted and in situ populations of the stellar halo, our result that blue GCs have an extreme tangential bias is an interesting counter-example to their result.

One possible explanation for the tangential orbits is that we are seeing a survival-bias effect, whereby GCs on radially biased orbits are more likely to be disrupted, as they reach more deeply into the center of the potential. However, for this scenario to work, the metal-poor GCs would have to be in place longer than the metal-rich GCs, contrary to the expectation that the former are accreted and the latter form in situ.

Another possibility would be a dynamical effect noted by Goodman & Binney (1984) whereby gradual accretion of mass at the center of a spherical system will preferentially circularize orbits in the outer regions.

The origin of this peculiar halo anisotropy remains an open question, deserving further study.

5.3. Stellar Mass Distribution

Since we have chosen to model the stellar mass of the galaxy as its own Sérsic profile, as opposed to a constant mass-to-light ratio multiplied by the enclosed luminosity, we have a handle on how the stellar mass distribution differs from the stellar light distribution. We find a half-mass effective radius of $26^{+4}_{-3}{}''$ ($2.7^{+0.5}_{-0.4}$ kpc when marginalizing over distance), much smaller than the B band half-light effective radius of $100''$ ($10.2^{+0.7}_{-0.7}$ kpc).

This relative concentration of the stellar mass is intriguingly similar to the situation at high redshift. van der Wel et al. (2014) used results from 3D-HST and CANDELS to trace the evolution in the stellar size–mass relation out to $z \sim 3$, finding a strong size evolution of ETGs at fixed mass of $R_e \propto (1 + z)^{-1.48}$. We compare our measurement of the stellar half-mass–radius with the ETG relations from van der Wel et al. (2014) in Figure 16. We see that the stellar mass distribution of NGC 1407 most closely matches the light distribution of compact galaxies at $z \sim 2$.

We note that our modeling may be biased toward smaller effective radii, as we are only fitting to the stellar mass surface density profile where we have data at $R < 100''$. If the mass-to-light profile does remain at a Milky Way-like value past $1 R_e$, then this would result in a less compact Sérsic fit than we find here.

6. Conclusions

We have presented a new analysis of the dynamics of the massive elliptical galaxy NGC 1407. We constrained the dynamical mass of the galaxy using a variety of data sets, including metal-rich and metal-poor GC velocity measurements, the stellar velocity dispersion measurements from longslit and multislit observations, and the spatially resolved mass-to-light ratio from stellar population models.

We found the following:

1. The DM virial mass and concentration are well matched to expectations from ΛCDM.
2. The DM halo of NGC 1407 likely has a cusp ($\gamma = 1$). This is shallower than expected for a normal ΛCDM halo with adiabatic contraction, although a larger sample size is needed to constrain the physical origin of this result.
3. The blue (metal-poor) GCs of NGC 1407 are on tangentially biased orbits (contrary to expectations for accreted stellar mass), while the red (metal-rich) clusters are on slightly radially biased orbits.
4. The stellar mass distribution is significantly more compact than the stellar luminosity distribution, reminiscent of compact "red nugget" galaxies at high redshift.

We are just beginning to probe the γ–M_{halo} relation in the regime of giant early-type galaxies. Here we have shown that it is feasible to populate this parameter space with individual galaxies, and we intend to follow up this work with a larger study of galaxies from the SLUGGS survey.

Appendix A
MCMC Sampling

Here, in Figures 17–19, we show the detailed results of our sampling of the posterior probability distribution for the model parameter space described in Section 3.
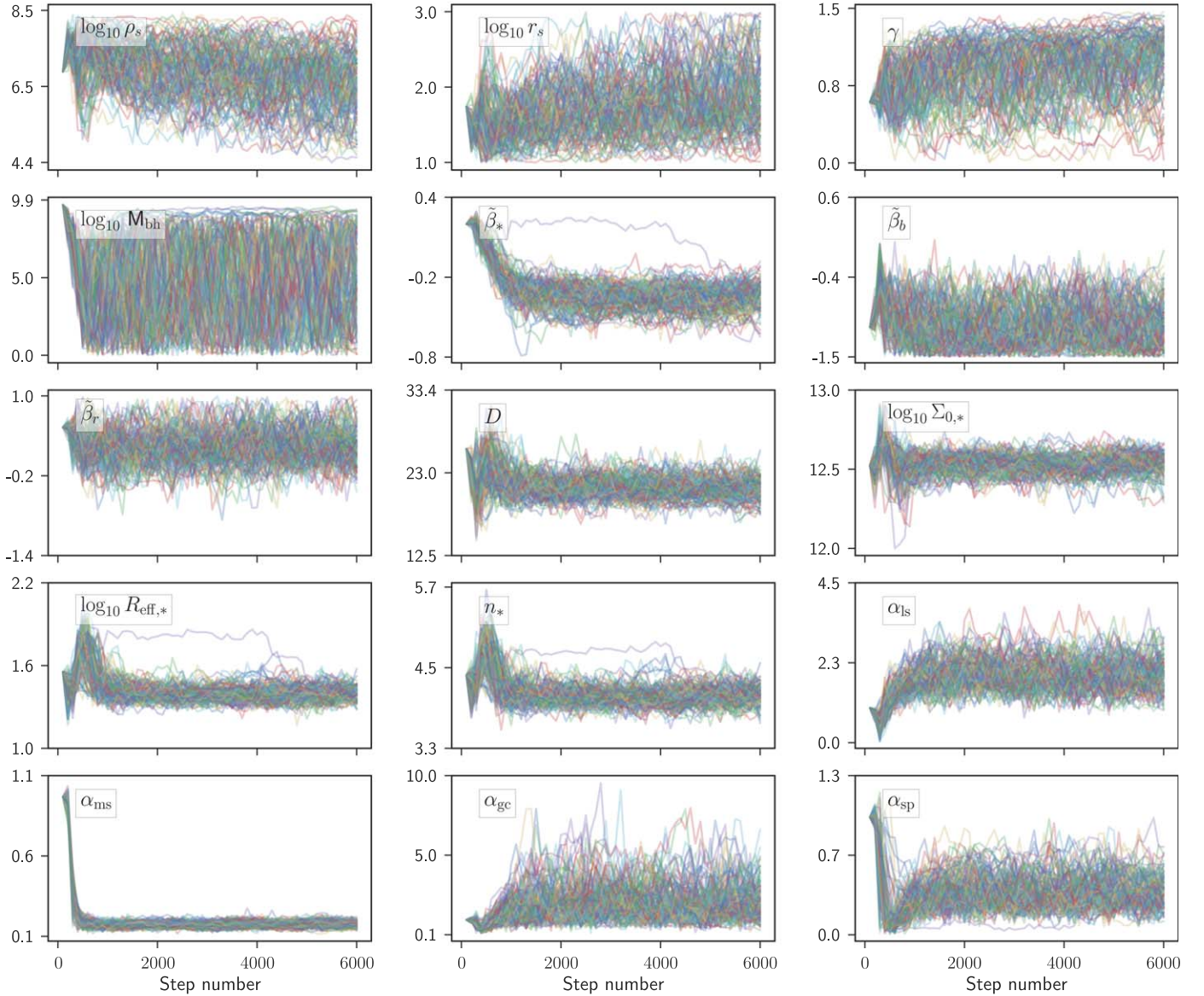

Figure 17. Walker traces across each iteration. Units are taken from Table 3. ρ_s, r_s, M_{bh}, $\Sigma_{0,*}$, and $R_{e,*}$ are shown as the logarithm (base 10) of those quantities, and the anisotropy parameters (β) are shown as the symmetrized anisotropy parameter, $\tilde{\beta} = -\log_{10}(1 - \beta)$. We reject the first 4500 walker steps in our analysis, where it is clear from the walker traces that the sampler has not yet converged.
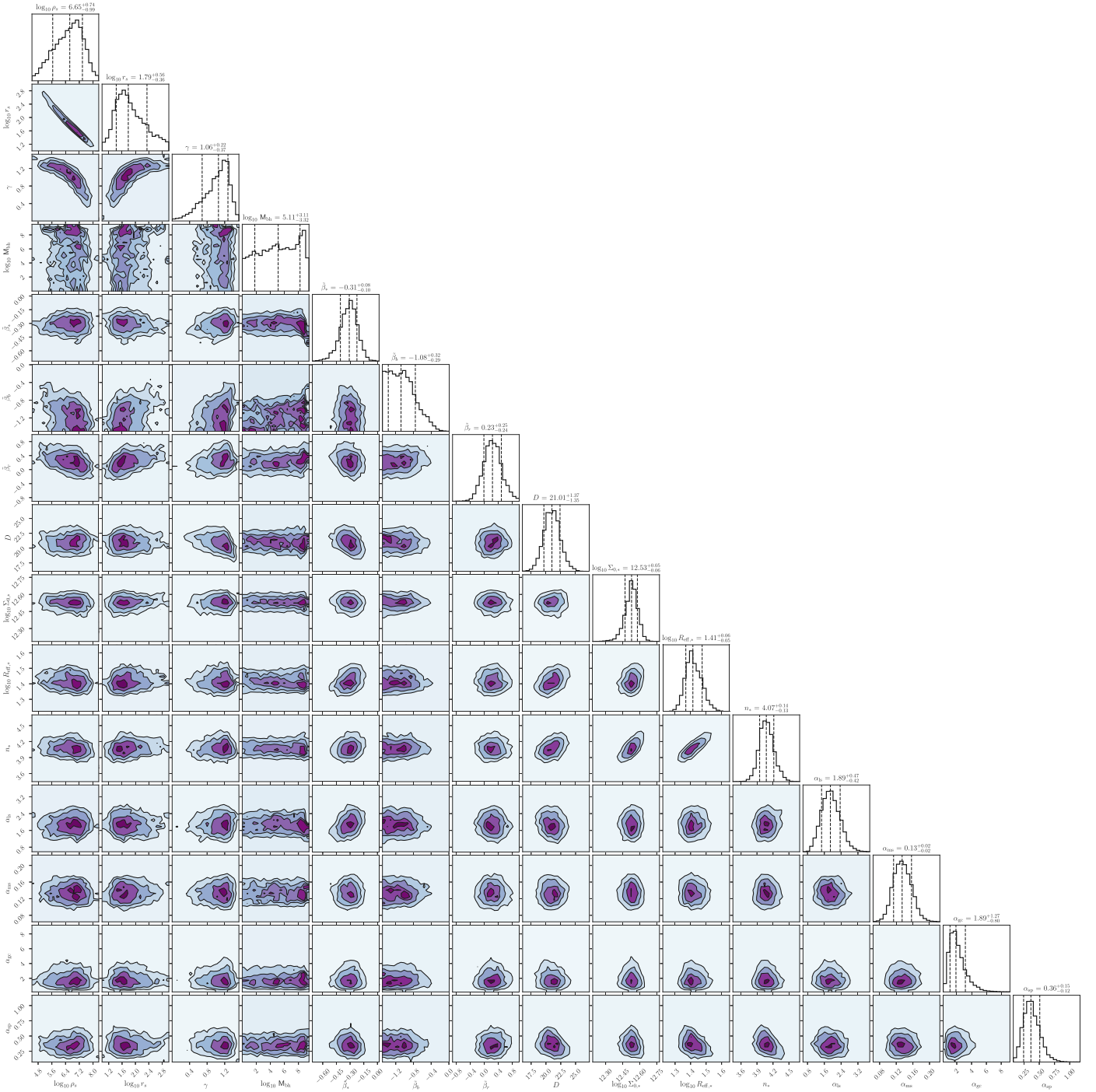
Figure 18. Posterior probability distribution for our model. Histograms along the diagonal show the marginalized posterior distributions for the respective parameters. The dashed vertical lines mark the 16th, 50th, and 84th percentiles. The contours (at levels equivalent to 0.5, 1, 1.5, and 2σ for a 2D Gaussian distribution) show the covariances between these parameters. We hit the prior bounds for $M_{\rm bh}$ and $\tilde{\beta}_b$. For the SMBH, we have very little constraints by design, so we restrict it to be less than $10^{11} M_{\odot}$. For all anisotropy parameters, we restrict the range to such that $-1.5 < -\log_{10}(1 - \beta)$ to avoid floating-point underflows. However, at such tangential orbital anisotropies, the physical differences in the dynamics are negligible.
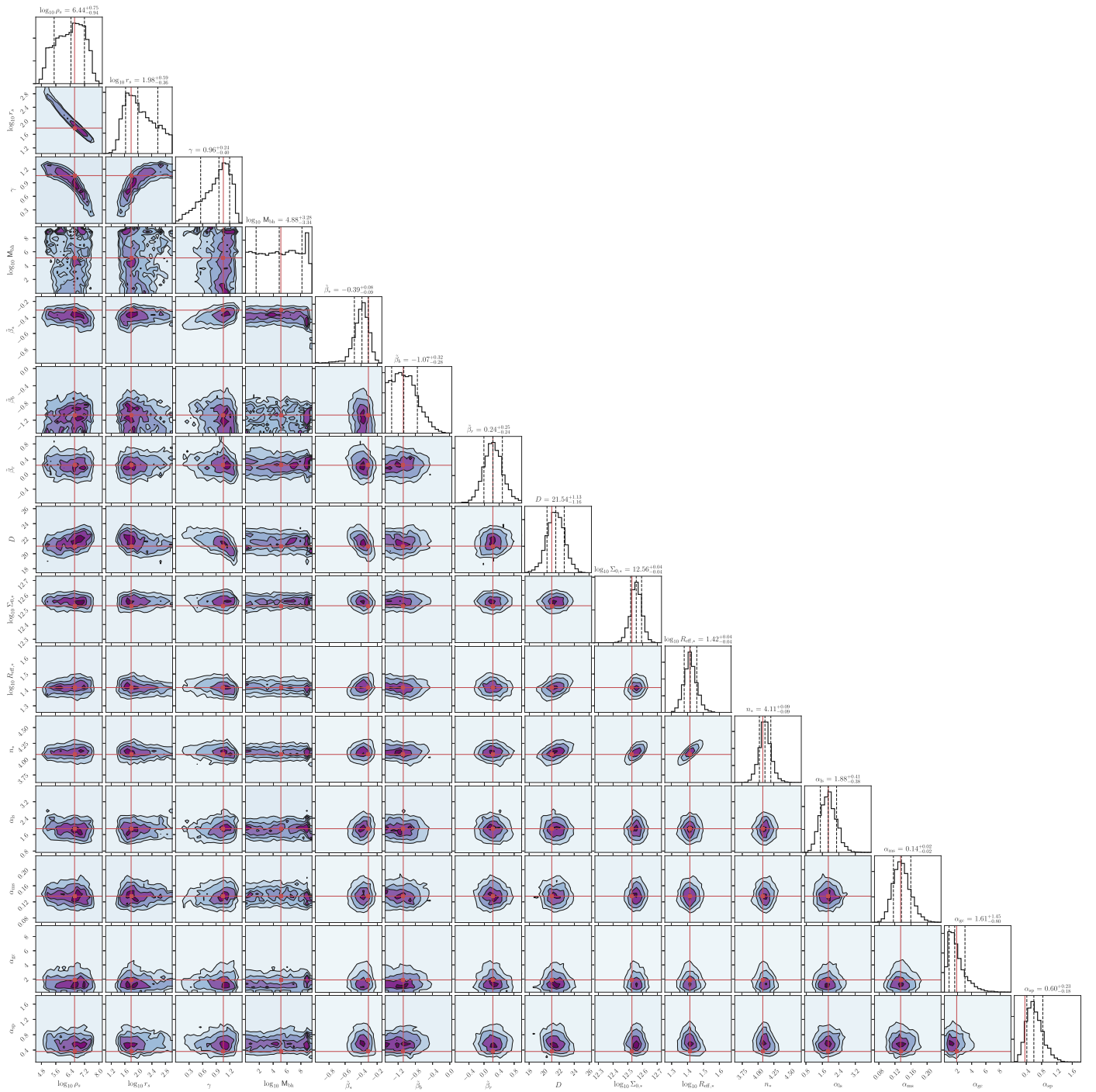
Figure 19. Posterior probability distribution for our model applied to the mock data, as discussed in Section 4.1.

Appendix B
Systematics Tests

We performed a number of tests to investigate the systematic uncertainty on the recovered DM halo parameters. For each of the tests described below, we plot a comparison of the DM halo parameter posterior distribution (re-parameterized $\log_{10}(M_{200}/M_\odot)$ and c_{200}) of the reference model described in the main text (in purple) with the distribution found when doing the specified test (in red). The contours are drawn at the 1 and 2 sigma levels.

B.1. Wide Distance Prior

We replaced our informative distance prior with a wide uniform distance prior, $D \sim \mathcal{U}(15\,\mathrm{Mpc}, 30\,\mathrm{Mpc})$. We recover a lower distance value ($\sim 17\,\mathrm{Mpc}$, compared to 21 Mpc with the informative prior). As shown in Figure 20, this has the effect of increasing the inner DM slope value, as the lower distance at fixed surface brightness results in a lower luminosity, and hence lower stellar mass and steeper DM density slope.

B.2. Masked Stellar Kinematic Data Set

We fit all stellar kinematic data, including those masked out as described in Section 2.3. We find a more concentrated halo and hence a lower value for γ (shown in Figure 21). We also find a slightly worse agreement of the multislit data with the model, as quantified by the weight hyperparameter α_{ms}, which changes from 0.13 to 0.10. While there is still work to be done to inference the presence and extent of substructure in stellar kinematic data, we thus find that an imperfect cut is better than no cut at all. However, the open question of whether or not the outer stellar halo of NGC 1407 is in entirely in equilibrium adds ~ 0.2 dex systematic uncertainty to the halo mass measurement and ~ 8 to that of the halo concentration measurement.

B.3. Varying Anisotropy Profiles

We performed similar mock data tests to those described in Section 3.4, but rather than using the constant anisotropy profile, we used a radially varying profile to generate the mock kinematic data. We ran one test where we replaced the stellar kinematic data with one generated using a Mamon & Łokas (2005) profile (shown in Figure 22). This model transitions from isotropic in the center to $\beta = 0.5$ in the outskirts, with the transition radius, r_a. Here we set $r_a = 10\,\mathrm{kpc}$ to be consistent with the value of $r_a = 0.018\,r_{\mathrm{vir}}$ from theory, e.g., Figure 2 from Mamon & Łokas (2005). We find a good recovery of the mass parameters, and we find the recovery of the stellar anisotropy to be isotropic to within the uncertainty.

We performed a similar test, but instead of replacing the stellar anisotropy profile, we replaced the red GC anisotropy profile with a Mamon & Łokas (2005) radially varying profile where we set $r_a = 56\,\mathrm{kpc}$. This value was chosen to lie in the range of $0.018 < r_a/r_{\mathrm{vir}} < 0.18$, where the lower bound was shown to be a good match to the stellar orbits from merger remnants and the upper bound was found to be a good match to the DM orbits for collisionless N-body simulations (Mamon & Łokas 2005). As shown in Figure 23, we found a notable difference in the recovered halo parameters, with c_{200} changing from 9 to 25 (and hence a lower value of γ and lower value of M_{200}). Given this difference, we emphasize that our findings
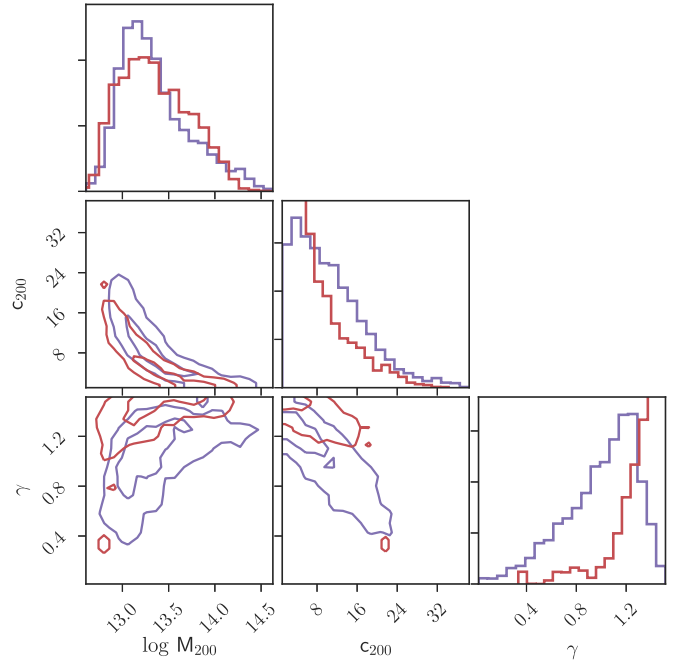

Figure 20. Comparison of the posterior probability distributions for the DM halo parameters. Purple contours show the reference inference, and the red contours show the inference with a wide uniform prior on the distance, between 15 and 30 Mpc.
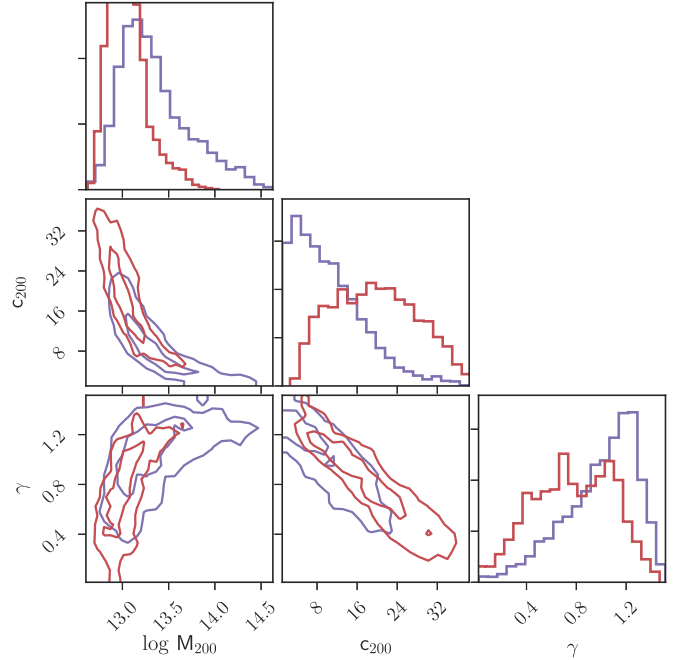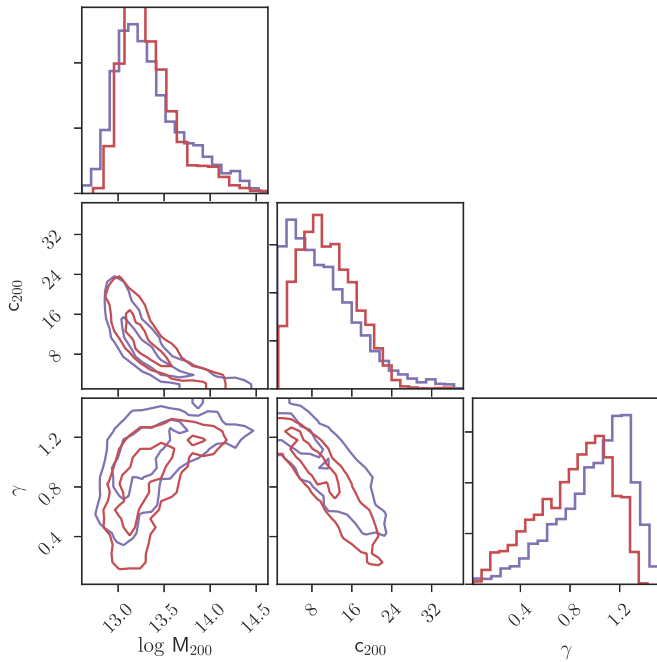

Figure 21. Comparison of the posterior probability distributions for the DM halo parameters. Purple contours show the reference inference, and the red contours show the inference when we do not mask any of the stellar kinematics data points.

are conditional on the adopted anisotropy profile. We defer the in-depth analysis of the GC anisotropy for future work.

B.4. Non-varying Υ_*

We removed our knowledge of the stellar population constraints for NGC 1407 and instead used a stellar mass

Figure 22. Comparison of the posterior probability distributions for the DM halo parameters. Purple contours show the reference inference, and the red contours show the recovery of the parameters when the stellar kinematics are generated with a Mamon & Lokas anisotropy profile.
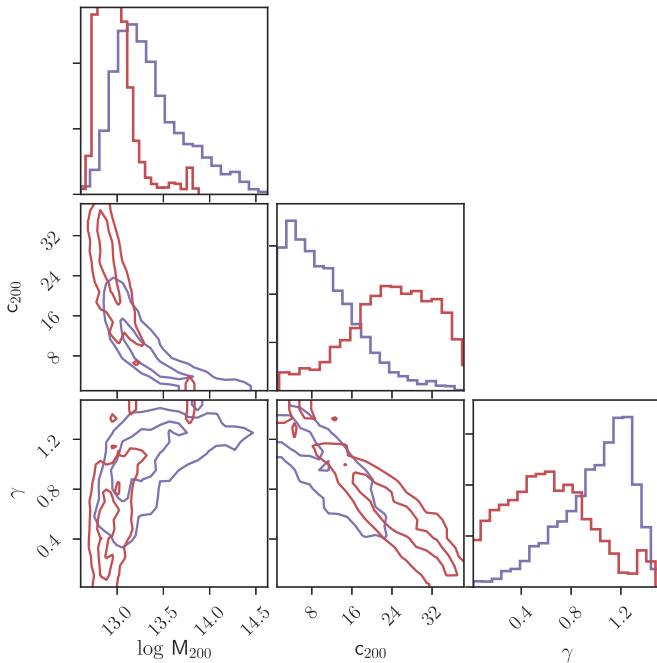

Figure 24. Comparison of the posterior probability distributions for the DM halo parameters. Purple contours show the reference inference, and the red contours show the inference assuming that the mass-to-light ratio (Υ_*) does not vary with radius.
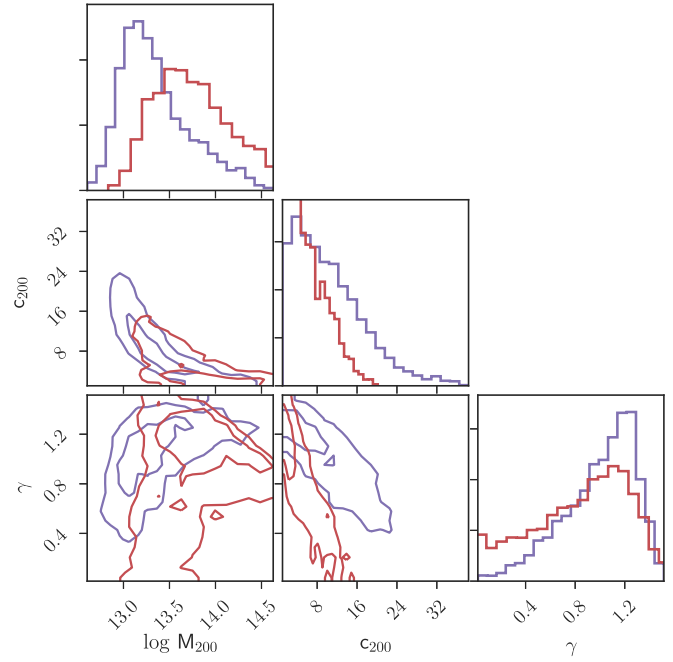

Figure 23. Comparison of the posterior probability distributions for the DM halo parameters. Purple contours show the reference inference, and the red contours show the recovery of the parameters when the red GC kinematics are generated with a Mamon & Lokas anisotropy profile.

model where $M_*(r) = \Upsilon_* L(r)$, using a fixed stellar surface brightness distribution given in Section 2.1. With this model we found weaker constraints on γ and a slightly higher value of the halo mass (shown in Figure 24). For the mass-to-light ratio we find $\Upsilon_{*,B} = 8.97^{+0.98}_{-1.08} \, M_\odot/L_{\odot,B}$ ($\Upsilon_{*,I} \sim 4 \, M_\odot/L_{\odot,I}$ when adopting the mean $B-I$ color from Spolaor et al. 2008).

ORCID iDs

Asher Wasserman ◉ https://orcid.org/0000-0003-4235-3595
Aaron J. Romanowsky ◉ https://orcid.org/0000-0003-2473-0369
Jean Brodie ◉ https://orcid.org/0000-0002-9658-8763
Pieter van Dokkum ◉ https://orcid.org/0000-0002-8282-9888
Charlie Conroy ◉ https://orcid.org/0000-0002-1590-8551
Alexa Villaume ◉ https://orcid.org/0000-0003-1887-0621
Jay Strader ◉ https://orcid.org/0000-0002-1468-9668
Sabine Bellstedt ◉ https://orcid.org/0000-0003-4169-9738

References

Adams, J. J., Simon, J. D., Fabricius, M. H., et al. 2014, ApJ, 789, 63
Agnello, A., Evans, N. W., Romanowsky, A. J., & Brodie, J. P. 2014, MNRAS, 442, 3299
Alabi, A. B., Forbes, D. A., Romanowsky, A. J., et al. 2017, MNRAS, 468, 3949
Arnold, J. A., Romanowsky, A. J., Brodie, J. P., et al. 2014, ApJ, 791, 80
Astropy Collaboration, Robitaille, T. P., Tollerud, E. J., et al. 2013, A&A, 558, A33
Bellstedt, S., Forbes, D. A., Foster, C., et al. 2017, MNRAS, 467, 4540
Binney, J., & Tremaine, S. 2008, Galactic Dynamics (2nd ed.; Princeton, NJ: Princeton Univ. Press)
Blumenthal, G. R., Faber, S. M., Flores, R., & Primack, J. R. 1986, ApJ, 301, 27
Boylan-Kolchin, M., Bullock, J. S., & Kaplinghat, M. 2011, MNRAS, 415, L40
Brodie, J. P., Romanowsky, A. J., Strader, J., et al. 2014, ApJ, 796, 52
Brodie, J. P., & Strader, J. 2006, ARA&A, 44, 193
Brough, S., Forbes, D. A., Kilborn, V. A., Couch, W., & Colless, M. 2006, MNRAS, 369, 1351
Buitrago, F., Trujillo, I., Curtis-Lake, E., et al. 2017, MNRAS, 466, 4888
Bullock, J. S., & Boylan-Kolchin, M. 2017, ARA&A, 55, 343
Cantiello, M., Blakeslee, J. P., Raimondo, G., et al. 2005, ApJ, 634, 239
Cappellari, M., & Emsellem, E. 2004, PASP, 116, 138
Chabrier, G. 2003, ApJL, 586, L133
Chemin, L., de Blok, W. J. G., & Mamon, G. A. 2011, AJ, 142, 109
Choi, J., Dotter, A., Conroy, C., et al. 2016, ApJ, 823, 102

Churazov, E., Tremaine, S., Forman, W., et al. 2010, MNRAS, 404, 1165
Ciotti, L., & Bertin, G. 1999, A&A, 352, 447
Conroy, C., & van Dokkum, P. G. 2012, ApJ, 760, 71
Conroy, C., Villaume, A., van Dokkum, P., & Lind, K. 2018, ApJ, 854, 139
Cooper, M. C., Newman, J. A., Davis, M., Finkbeiner, D. P., & Gerke, B. F. 2012, spec2d: DEEP2 DEIMOS Spectral Pipeline, Astrophysics Source Code Library, ascl:1203.003
Das, P., Gerhard, O., Churazov, E., & Zhuravleva, I. 2010, MNRAS, 409, 1362
de Vaucouleurs, G., de Vaucouleurs, A., Corwin, H. G., Jr., et al. 1991, Third Reference Catalogue of Bright Galaxies, Vol. I: Explanations and References, Vol. II: Data for Galaxies Between 0^h and 12^h, Vol. III: Data for Galaxies Between 12^h and 24^h (New York: Springer)
Deason, A. J., Belokurov, V., Evans, N. W., & McCarthy, I. G. 2012, ApJ, 748, 2
Dekel, A., Devor, J., & Hetzroni, G. 2003, MNRAS, 341, 326
Dekel, A., Stoehr, F., Mamon, G. A., et al. 2005, Natur, 437, 707
Di Cintio, A., Tremmel, M., Governato, F., et al. 2017, MNRAS, 469, 2845
Dutton, A. A., & Macciò, A. V. 2014, MNRAS, 441, 3359
Dutton, A. A., Macciò, A. V., Stinson, G. S., et al. 2015, MNRAS, 453, 2447
El-Zant, A. A., Hoffman, Y., Primack, J., Combes, F., & Shlosman, I. 2004, ApJL, 607, L75
Faber, S. M., Phillips, A. C., Kibrick, R. I., et al. 2003, Proc. SPIE, 4841, 1657
Flores, R. A., & Primack, J. R. 1994, ApJL, 427, L1
Forbes, D. A., Alabi, A., Brodie, J. P., et al. 2017, AJ, 153, 114
Forbes, D. A., Ponman, T., & O'Sullivan, E. 2012, MNRAS, 425, 66
Forbes, D. A., Sánchez-Blázquez, P., Phan, A. T. T., et al. 2006, MNRAS, 366, 1230
Foreman-Mackey, D., Hogg, D. W., Lang, D., & Goodman, J. 2013, PASP, 125, 306
Foster, C., Pastorello, N., Roediger, J., et al. 2016, MNRAS, 457, 147
Gnedin, O. Y., Kravtsov, A. V., Klypin, A. A., & Nagai, D. 2004, ApJ, 616, 16
Goodman, J., & Binney, J. 1984, MNRAS, 207, 511
Goodman, J., & Weare, J. 2010, Comm. App. Math. Comp. Sci., 5, 65
Harris, W. E., Ciccone, S. M., Eadie, G. M., et al. 2017, ApJ, 835, 101
Hobson, M. P., Bridle, S. L., & Lahav, O. 2002, MNRAS, 335, 377
Humphrey, P. J., Buote, D. A., Gastaldello, F., et al. 2006, ApJ, 646, 899
Hunter, J. D. 2007, CSE, 9, 90
Jarrett, T. H., Chester, T., Cutri, R., et al. 2000, AJ, 119, 2498
Jones, E., Oliphant, T., Peterson, P., et al. 2001, SciPy: Open Source Scientific Tools for Python
Kafle, P. R., Sharma, S., Lewis, G. F., & Bland-Hawthorn, J. 2012, ApJ, 761, 98
Kafle, P. R., Sharma, S., Robotham, A. S. G., Elahi, P. J., & Driver, S. P. 2018, MNRAS, 475, 4434
Klypin, A., Kravtsov, A. V., Valenzuela, O., & Prada, F. 1999, ApJ, 522, 82
Laporte, C. F. P., & White, S. D. M. 2015, MNRAS, 451, 1177
Li, H., Ge, J., Mao, S., et al. 2017, ApJ, 838, 77
Lima Neto, G. B., Gerbal, D., & Márquez, I. 1999, MNRAS, 309, 481
Ma, Y.-Z., & Berndsen, A. 2014, A&C, 5, 45
Mamon, G. A., & Łokas, E. L. 2005, MNRAS, 363, 705
Martín-Navarro, I., Barbera, F. L., Vazdekis, A., Falcón-Barroso, J., & Ferreras, I. 2015, MNRAS, 447, 1033
Martizzi, D., Teyssier, R., & Moore, B. 2013, MNRAS, 432, 1947
Mashchenko, S., Wadsley, J., & Couchman, H. M. P. 2008, Sci, 319, 174
McConnell, N. J., Chen, S.-F. S., Ma, C.-P., et al. 2013, ApJL, 768, L21
McConnell, N. J., Lu, J. R., & Mann, A. W. 2016, ApJ, 821, 39
McKinney, W. 2010, in Proc. IX Python in Science Conf., ed. S. van der Walt & J. Millman (Austin, TX: SciPy), 51
Merritt, D. 1985, MNRAS, 214, 25P
Mitzkus, M., Cappellari, M., & Walcher, C. J. 2017, MNRAS, 464, 4789
Moore, B., Ghigna, S., Governato, F., et al. 1999, ApJL, 524, L19
Napolitano, N. R., Pota, V., Romanowsky, A. J., et al. 2014, MNRAS, 439, 659
Napolitano, N. R., Romanowsky, A. J., Coccato, L., et al. 2009, MNRAS, 393, 329
Napolitano, N. R., Romanowsky, A. J., & Tortora, C. 2010, MNRAS, 405, 2351
Navarro, J. F., Eke, V. R., & Frenk, C. S. 1996, MNRAS, 283, L72
Navarro, J. F., Frenk, C. S., & White, S. D. M. 1997, ApJ, 490, 493
Newman, A. B., Treu, T., Ellis, R. S., et al. 2013a, ApJ, 765, 24

Newman, A. B., Treu, T., Ellis, R. S., & Sand, D. J. 2013b, ApJ, 765, 25
Newman, J. A., Cooper, M. C., Davis, M., et al. 2013c, ApJS, 208, 5
Novak, G. S., Cox, T. J., Primack, J. R., Jonsson, P., & Dekel, A. 2006, ApJL, 646, L9
Oh, S.-H., de Blok, W. J. G., Brinks, E., Walter, F., & Kennicutt, R. C., Jr. 2011, AJ, 141, 193
Oldham, L., & Auger, M. 2018, MNRAS, 474, 4169
Oldham, L. J., & Auger, M. W. 2016, MNRAS, 457, 421
Oldham, L. J., & Auger, M. W. 2018, MNRAS, 476, 133
Oñorbe, J., Domínguez-Tenreiro, R., Sáiz, A., & Serna, A. 2007, MNRAS, 376, 39
Oser, L., Ostriker, J. P., Naab, T., Johansson, P. H., & Burkert, A. 2010, ApJ, 725, 2312
Paggi, A., Kim, D.-W., Anderson, C., et al. 2017, ApJ, 844, 5
Pastorello, N., Forbes, D. A., Foster, C., et al. 2014, MNRAS, 442, 1003
Pedregosa, F., Varoquaux, G., Gramfort, A., et al. 2011, JMLR, 12, 2825
Peirani, S., Dubois, Y., Volonteri, M., et al. 2017, MNRAS, 472, 2153
Peng, E. W., Jordán, A., Côté, P., et al. 2006, ApJ, 639, 95
Pérez, F., & Granger, B. E. 2007, CSE, 9, 21
Pineda, J. C. B., Hayward, C. C., Springel, V., & Mendes de Oliveira, C. 2017, MNRAS, 466, 63
Planck Collaboration, Ade, P. A. R., Aghanim, N., et al. 2016, A&A, 594, A13
Poci, A., Cappellari, M., & McDermid, R. M. 2017, MNRAS, 467, 1397
Pontzen, A., & Governato, F. 2012, MNRAS, 421, 3464
Pota, V., Brodie, J. P., Bridges, T., et al. 2015, MNRAS, 450, 1962
Pota, V., Forbes, D. A., Romanowsky, A. J., et al. 2013, MNRAS, 428, 389
Prieto, J. L., & Gnedin, O. Y. 2008, ApJ, 689, 919
Proctor, R. N., Forbes, D. A., Romanowsky, A. J., et al. 2009, MNRAS, 398, 91
Quintana, H., Fouque, P., & Way, M. J. 1994, A&A, 283, 722
Robles, V. H., Lora, V., Matos, T., & Sánchez-Salcedo, F. J. 2015, ApJ, 810, 99
Rocha, M., Peter, A. H. G., Bullock, J. S., et al. 2013, MNRAS, 430, 81
Rodriguez-Gomez, V., Pillepich, A., Sales, L. V., et al. 2016, MNRAS, 458, 2371
Rodríguez-Puebla, A., Primack, J. R., Avila-Reese, V., & Faber, S. M. 2017, MNRAS, 470, 651
Romanowsky, A. J., & Kochanek, C. S. 2001, ApJ, 553, 722
Romanowsky, A. J., Strader, J., Spitler, L. R., et al. 2009, AJ, 137, 4956
Röttgers, B., Naab, T., & Oser, L. 2014, MNRAS, 445, 1065
Rusli, S. P., Thomas, J., Saglia, R. P., et al. 2013, AJ, 146, 45
Salpeter, E. E. 1955, ApJ, 121, 161
Schaller, M., Frenk, C. S., Bower, R. G., et al. 2015a, MNRAS, 451, 1247
Schaller, M., Frenk, C. S., Bower, R. G., et al. 2015b, MNRAS, 452, 343
Schuberth, Y., Richtler, T., Hilker, M., et al. 2010, A&A, 513, A52
Shen, J., & Gebhardt, K. 2010, ApJ, 711, 484
Simon, J. D., Bolatto, A. D., Leroy, A., & Blitz, L. 2003, ApJ, 596, 957
Sonnenfeld, A., Treu, T., Marshall, P. J., et al. 2015, ApJ, 800, 94
Spekkens, K., Giovanelli, R., & Haynes, M. P. 2005, AJ, 129, 2119
Spolaor, M., Forbes, D. A., Hau, G. K. T., Proctor, R. N., & Brough, S. 2008, MNRAS, 385, 667
Su, Y., Gu, L., White, R. E., III, & Irwin, J. 2014, ApJ, 786, 152
Su, Y., & Irwin, J. A. 2013, ApJ, 766, 61
Thomas, J., Saglia, R. P., Bender, R., et al. 2007, MNRAS, 382, 657
Tollet, E., Macciò, A. V., Dutton, A. A., et al. 2016, MNRAS, 456, 3542
Tully, R. B., Courtois, H. M., Dolphin, A. E., et al. 2013, AJ, 146, 86
van der Wel, A., Franx, M., van Dokkum, P. G., et al. 2014, ApJ, 788, 28
van Dokkum, P., Conroy, C., Villaume, A., Brodie, J., & Romanowsky, A. J. 2017, ApJ, 841, 68
Villaume, A., Conroy, C., Johnson, B., et al. 2017, ApJS, 230, 23
Walker, M. G., & Peñarrubia, J. 2011, ApJ, 742, 20
Walt, S. v. d., Colbert, S. C., & Varoquaux, G. 2011, CSE, 13, 22
Wang, W., Han, J., Cole, S., et al. 2018, MNRAS, 476, 5669
Watkins, L. L., Evans, N. W., & An, J. H. 2010, MNRAS, 406, 264
Xu, D., Springel, V., Sluse, D., et al. 2017, MNRAS, 469, 1824
Zhang, H.-X., Peng, E. W., Côté, P., et al. 2015, ApJ, 802, 30
Zhang, Z., Xu, H., Wang, Y., et al. 2007, ApJ, 656, 805
Zhu, L., Long, R. J., Mao, S., et al. 2014, ApJ, 792, 59
Zhu, L., Romanowsky, A. J., van de Ven, G., et al. 2016, MNRAS, 462, 4001